UNIVERSITY OF CALIFORNIA, SAN DIEGO

Comparison of Shape Reconstruction Strategies in a Complex Flexible Structure

A Thesis submitted in partial satisfaction of the requirements
for the degree Master of Science

in

Structural Engineering

by

Zhu Mao

Committee in charge:

Professor Michael D. Todd, Chair
Professor Hyonny Kim
Professor P. Benson Shing

2008

The Thesis of Zhu Mao is approved, and it is acceptable

in quality and form for publication on microfilm:

_____

_____

_____

Chair

University of California, San Diego

2008

TABLE OF CONTENTS

LIST OF FIGURES

LIST OF TABLES

ACKNOWLEDGEMENTS

The very first one that I would like to thank gratefully is my advisor, Michael Todd, who gave me the opportunity to work in this team and guided me on my subsequent research. His nice instruction, creative fervor and intelligence always encouraged me, and helped me, both in academic and personal life. Without him, I would definitely not be where I am at this moment.

I would also like to thank my committee members, P. Benson Shing and Hyonny Kim, for their guidance, suggestion, and kind help.

Thanks to my friends and collaborators in the group, who helped me from being a freshman of the new western world, in improving my communication skills, in getting use to the unfamiliar environment, and in learning and enriching my knowledge of the real culture and society where there is a big difference from my previous experiences.

I would like to acknowledge Brandon J. Arritt, Deputy Program Manager of Integrated Structural Systems, Air Force Research Laboratory, Kirtland AFB, Albuquerque, NM, for providing the initial ABAQUS finite element model studied in my work.

Most importantly, I want to give my special thanks to my wife, Ling, for her everlasting love, understanding and support.

ABSTRACT OF THE THESIS

Comparison of Shape Reconstruction Strategies in a Complex Flexible Structure

by

Zhu Mao

Master of Science in Structural Engineering

University of California, San Diego, 2008

Professor Michael D. Todd, Chair

Current control and performance requirements for large-aperture deployable structures call for precise displacement control, with some tolerances approaching micron levels. Given that strain gages are one of the most economically-deployed sensor architectures, we explored two methods for reconstructing displacement from a distributed strain sensing array. One method linearly maps displacement fields to local strains in a supervised learning mode. After loading the system with sufficient cases, a matrix can be established to approach the approximate displacement-strain relationship. The other method is based on linear regression of generalized basis function projections, typically mode shapes. Results of these two approaches are compared for accuracy, robustness, training time, and real-time feasibility. The second method has higher accuracy due to natural modal behaviors, while the first method is feasible if large amount of training cases and measuring points are available.

1. Introduction and Background

1.1. Space Application Needs and Requirements

The development of large span structures has received increasing attention in the Department of Defense in recent years for the potential of these frames to carry devices such as optical telescopes, interferometers, and high-precision microwave and radar antennas, and improve the quality of space communication. [1][26] However, due to the large inertia and high flexibility of the space-based large span trusses, large thermal gradients of the cosmic environment, and even many local influences such as debris or micrometeoroid impacts, these structures will have deformation that cannot be ignored in orbit with regard to precise positioning and control for required communications performance. As such, this deformation becomes one of the major reasons of degradation of communication quality, and one possible method to deal with this issue is software compensation, which requires accurate on-orbit geometric configurations. The shape sensing techniques to be performed in compensation of communication process must conform the lambda over 20 rule, which means error of the metrology system should be less than lambda/20 RMS. Specifically for radar platform, where the boom has a dimension of hundreds of meters, to have the acceptable communication quality, the in-situ error of shape reconstruction should be less than 1 millimeter over the entire span, which is a challenging task. [1]

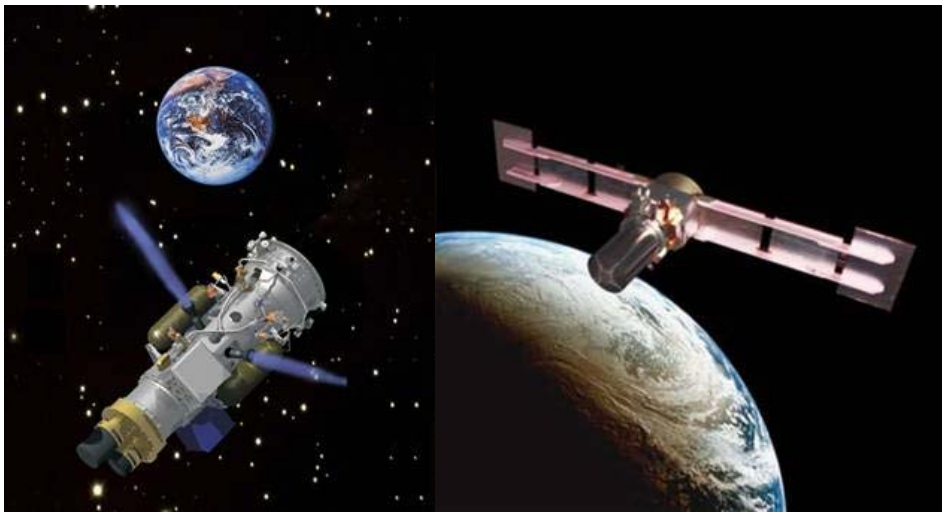

Figure 1: space facilities

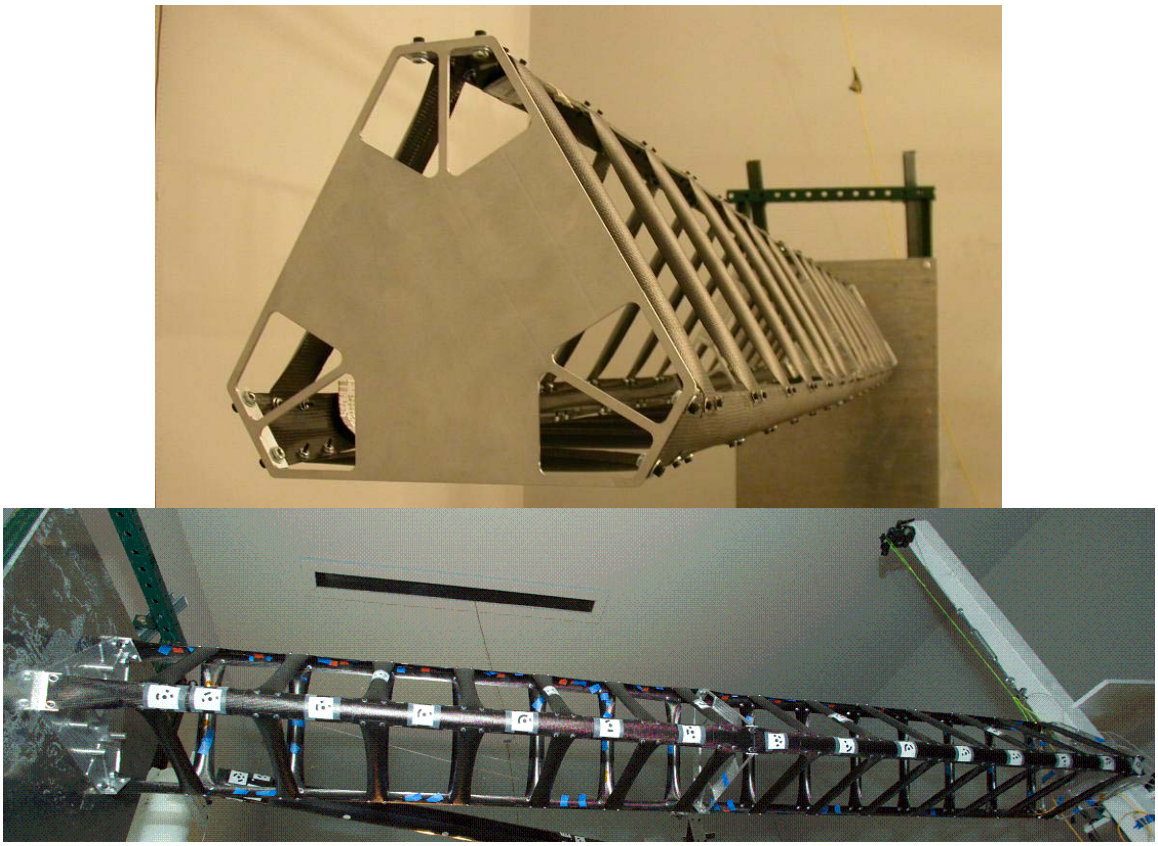

Figure 2: long span aperture truss (picture courtesy of B. J. Arritt, Air Force Research Laboratory, Kirtland AFB, NM.)

1.2. Scope and Contribution of the thesis

A complete solution to state awareness (and more specifically, shape reconstruction) problems necessarily requires investigation into both hardware (sensor) and algorithm issues. In this work, we shall assume that distributed local strain measurements, such as those obtained from a Bragg grating sensor array, are available. Subsequently, in this thesis we shall develop and compare two strategies for shape reconstruction of the large span flexible truss: a simplified neural network approach (linearization that becomes a matrix map) and mechanics-based basis functions approach (that uses finite sets of three-dimensional modal functions). The first approach is a training-based approach that requires a set of pre-deployment training cases to span the expected response range and then uses the trained “map”, which may be inverted in a pseudo-inverse sense due to linearity, to use as a displacement predictor. The second

approach does not require training and relies on explicit modeling of strain and displacement relationships. Each method requires a few “tuning” parameters, and the effects of the parameters are studied in detail as the two approaches are compared as possible algorithm candidates for real-time shape reconstruction of complex flexible structures.

The main contribution of this thesis is that a comparative study is performed on two methods that seek to map a finite, distributed strain field to global displacement (a form of inverse problem). Highly simplified versions of these approaches, particularly the mechanics approach, have been used before for one- and two-dimensional structures where much more explicit models have been developed, but nothing has been considered for full three-dimensional motion where exact models are not available. This contribution is made in light of several constraints placed on the problem such as no full-field measurement technique is allowed (i.e., the technique must rely only upon in-situ components), the technique must have flight qualification promise (primarily a hardware issue), and extraordinarily challenging goals in terms of spatial resolution are desirable.

1.3. Current Truss Model Description

A scaled model of such a truss structure that supports these activities is shown in Figure 2. The model is composed of several basic components (shown in Figure 3), which are connected in a global assembling topology (for convenience, we label each of the component as shown in Figure 4). There are five floors in the structure with equilateral triangular frame on each floor (shown in Figure 4), which makes the frame stable and well loadable. SMA (shape memory alloy) strips are adopted at certain bend edges of the longeron unit to create actuation points that make the frame deployable. Geometrical parameters and boundary conditions are listed in Table 1.

Table 1: geometrical dimension and boundary

Cross section	equilateral triangular		Number of floors	5
Side length	0.78 m		Total height	2.28 m
Batten width	36.8 mm		Longeron width	49.6 mm
Bottom B.C.	fixed		Top B.C.	free

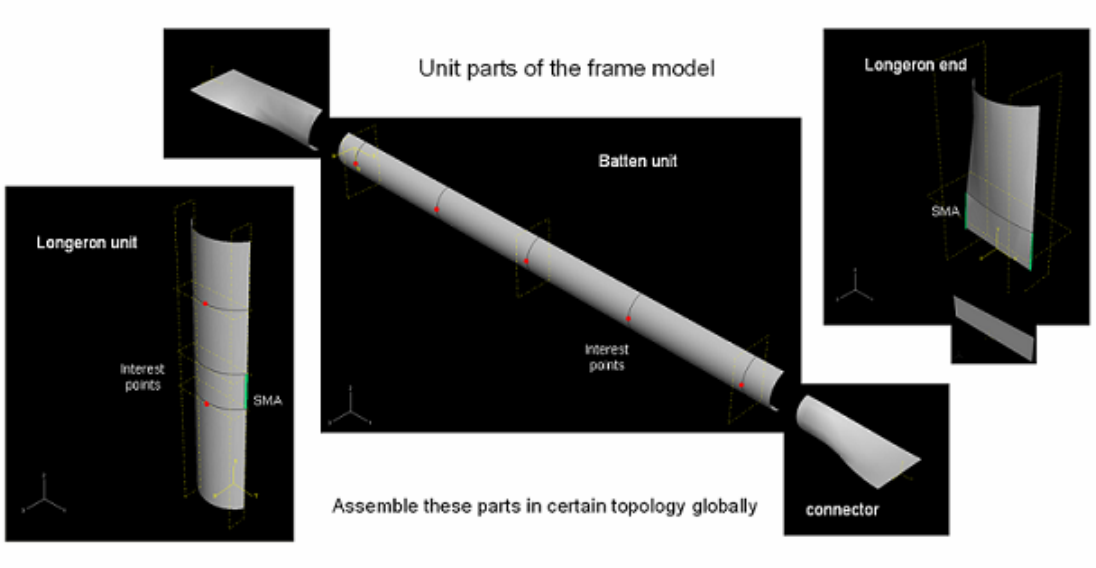

Figure 3: components of the structure

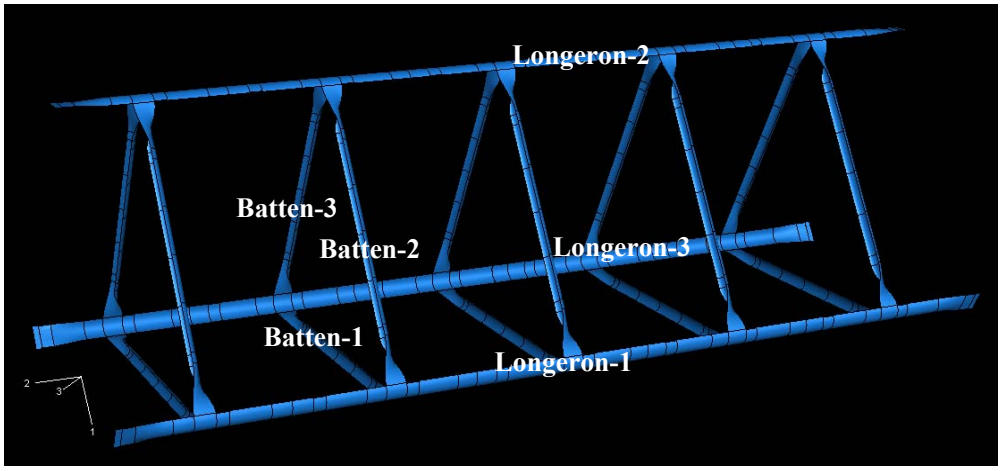

Figure 4: label of each component

It is assumed that the materials of frame are linear and elastic, and the parameters are shown in Table 2. It is also assumed that all loading situations cause only small deformations.

Table 2: material properties

Name	IM7/977-2 UNI	NiTi (SMA)
type	lamina	isotropic
density	ρ=1630 kg/m^3	ρ=6450 kg/m^3
Young's modulus	E_1=1.73E+011 Pa	E=7.5E+010 Pa
	E_2=9.17E+009 Pa	
Poisson's ratio	ν_{12}=0.34	ν=0.3
Shear modulus	G_{12}=5.65E+009 Pa	-

2. Shape Reconstruction Approaches

2.1. Previous Work Review

Previous work in shape reconstruction strategies may be classified into either of two classes of methods--non-contact and contact--depending upon implementation. In the non-contact regime, data are acquired via remote sensing means, typically optical methods, with no direct contact with the structure. F. Chen et al. provided an overview of non-contact 3-D shape reconstructions, [8] and in this reference, the surveyed optical techniques include:

- Time in Flight: This method is based on the time measured in flight of a laser or other light sources. To determine the distance of a target surface, the time difference between the arrival of an object pulse which is reflected back and a reference pulse which passes through an optical fiber is measured and then converted to distance.

- Laser Scanning: This technique is based on the triangulation relationship in optics, and digitizes the scanned point laser image by charged couple device (CCD), or a position sensitive detector (PSD).

- Moiré: The key to this technique is a master grating and a reference grating. From the two gratings, contour fringes can be generated and then resolved by a CCD camera.

- Laser Speckle Pattern Sectioning: This method uses 3-D Fourier transform relationship between distance space (range domain) and optical wavelength space (frequency domain) for object shape sensing. The Laser Speckle Pattern Sectioning, actually laser radar 3-D imaging is obtained by utilizing the correspondence of the two spaces.

- Interferometry: In this method, the fringes are formed by variation of the sensitivity matrix relating the geometry of an object with measured optical phases. There are three variables in the matrix: wavelength, refractive index, and illumination and observation directions, which can

derive three methods respectively: multiple wavelength, refractive index change, and illumination direction variation. Moreover, using frequency shift, double heterodyne interferometry, with better accuracy, can be deployed.

- Photogrammetry: This method usually requires bright markers such as retroreflective painted dots or pieces of glistening tape on the surface of measured object, and the shape reconstruction is established on the bundle adjustment principle.

- Laser Tracking System: The device of Laser Tracker is a combination of an interferometer for measuring distances and two high accuracy angle encoders for determining vertical and horizontal angles.

- Structured Light: This method is also categorized as active triangulation, and includes both projected coded light and sinusoidal fringe techniques.

By choosing suitable optical sources, implementing an adequate technique, and transforming local coordinates to the global coordinate systems, the shape of object can be reconstructed. This shape sensing process has various applications such as: intelligent structure control, obstacle detection, reverse engineering, orthopedics, geotechnical exploration, etc. [9] [10] [20]

For example, in reference [11] and [12], Radio Frequency (RF) was selected as the optical source. The RF-based sensor is also called the Autonomous Formation Flying (AFF) sensor, and this realize the deep space precision formation flying by measuring the relative range and bearing angles between multiple spacecrafts. For 1 km separations between two spacecrafts, AFF sensor has an excellent accuracy in real-time for both range and bearing angle measurements (2 cm and 1 arcmin). [11] Another application of AFF modules was implemented on control of a 25-Meter Aperture Virtual Structure Gossamer Telescope, and inter-module relative position and velocity vectors were estimated. [12]

More application on space structure, which utilized an eye-safe laser for its optical source, and a laser range scanner (LARS) was established as a precision measurement tool in space structures, with a short-medium range 3-D sensing capability (between 0.5 and 2000 m). The camera in this LARS can

address any spatial location within the field of 30×30 degrees of view in searching and measuring target. In this LARS application, target-based, feature-based, and image-based measurements are all allowed. [4]

In the area of reverse engineering and computer aided design (CAD), C. Reich et al. proposed a technique that combines photogrammetry and fringe projection. In their work, the shape of a car's door was determined by combining the phase-shift method for fringe measurement with a photogrammetric triangulation to calculate the 3-D coordinates of each measuring point on the surface. [5] With the similar approach, cloud of points was generated in Azernikov and Fischer's work, and surface information was reconstructed to build up the solid model. [13]

The non-contact measurement techniques can be used in remote sensing and geodetic survey. In optical remote sensing, solar radiation in different wavelength regions is detected, after reflection and scattering, photographs are taken by equipments located high up in space. In this application, sun light is the optical source. Many kinds of information will be acquired, including the broad shape of the earth's surface, and detailed shape of a certain building.

After reviewing the non-contact sensing techniques in structure shape reconstruction, the remaining techniques may be denoted as contact-based, which means that sensors are physically mounted onto the structures in the data acquisition process, with data and/or power conveyed either in wired or wireless modes. Wired modes are more mature, but wireless communications protocols, energy harvesting strategies, and efficient computing and transmission have significantly advanced wireless transmission in order to realize long distance data acquisition. [18]

For shape sensing in contact regime, Moll, M. et al. presented results on shape reconstruction of an unknown smooth convex 2-D plate using two tactile sensors, without requiring object immobilization. [14] In this process, two flat palms covered with tactile sensors manipulated the object, and there is one rotational degree of freedom at the joint of two palms. By tracking the contact points via tactile sensors, the outline curve of the plate can be determined, when the angle of two palms changes. Another example of wired sensing in shape reconstruction was from Luna Innovations Incorporated and Boeing, that, the shape of Variable Geometry Chevron (VGC) system at take-off was reconstructed from high density distributed

strain fiber mounted on the surface of the chevron. On each chevron, there are a set of three strain gages attached, and consider the simple model with only bending effective, the tip position (shape) can be estimated by geometrically calculating and integrating the strain data. [15]

In the contact problems, wireless sensing has emerged as a promising technology that could greatly impact the field of structural sensing and monitoring. [16] Some work about on-ground structural health monitoring (SHM) has utilized the remote sensing techniques, and a wireless intelligent sensor network was established, which combined sensor, A/D converter, microprocessor, wireless transmitter and power supply together. [17][18]

In summary, each non-contact and contact method has its own advantages. The non-contact methods require optical equipment, such as cameras to be fixed and adjusted apart from the structure itself, which requires extra on-orbit observer platforms whose controllability itself adds significant complication. The other method is inherently in-situ, using sensor array to capture certain information and then mapping those signals/measurements to the 3-D coordinates of the structure. Related with the present research scope involving the space truss, an in-situ technique is self-contained, although the possibility of weight addition to the deployed platform by sensor nodes and/or cables must be considered.

With the goal of designing “state aware” space structures in a lower-cost and lighter-weight, optical fiber sensors, especially fiber Bragg gratings, are a strongly-suited candidate for comprising a contact-category shape reconstruction strategy [1][2]. The most significant well-known advantages of fiber optical sensing include very high resolution (sub-micron sensitivity) [3], insensitivity to electromagnetic interference, negligible cabling weight, self-telemetry (the sensor is encoded directly into the cabling), and easy inline multiplexing. [7] For more information, reference [19] ~ [22] provide a comprehensive review of sensor network and fiber optical sensor technology.

Friebele et al. reviewed the results of some work at the Naval Research Laboratory where optical fiber strain sensors have been used on spacecraft structures, [2] and related work on a small cantilever

deployable boom was implemented by Blandino et al. using FBG strain sensors to obtain longitudinal deformation. [6] Moreover, with the outstanding performance of fiber Bragg gratings in metrology, shape sensing strategies on a similar boom to the task structure in this thesis (shown in Figure 2) are being considered at the Air Force Research Laboratory at Kirtland Air Force Base. [1] Using this test structure model as a platform, this work considers some candidate approaches for completing this shape reconstruction algorithm strategy.

Reconstruction algorithm is the important connection from data acquisition to the shape estimation. There are mainly three types of data processing algorithm in doing structural shape rebuilding: mathematical integration, artificial neural network, and model resolution.

The most straight forward method for displacement estimation is to integrate the strain measurements. In reference [23], the in-plane strains were obtained from a highly accurate measurement via wavelength-multiplexed fiber optic Bragg gratings. Assumed the mid-plane strain to be zero, or measured the top and bottom surface and solved mid-plane strain, which was due to axial stretching; then fitting the discrete strain data, and integrated twice to get displacement, an average RMS error of 0.025” was achieved. Kirby et al. directly calculated the integration approximating the strain-displacement relationships, with a polynomial representation of the strain field. [28] Similar approach of integration to reconstruct displacement in simple structures can be found in reference [6] and [15].

Some researchers regarded the shape sensing procedure as an artificial neural network, in both optical (non-contact) and strain measuring (contact) implementations. For example, Ganotra et al. used a feed-forward back propagation neural network in fringe projection profilometry for reconstruction of 3-D objects. There was a grating structure comprising two regions of different spatial periods, and the shape was reconstructed with the help of neural networks using images of the projected grating. [24] In reference [25], deformable self-organizing feature map (SOFM) was used on the morphing techniques by Igwe, P.C., et al., which is a skeletal framework for modeling object surfaces that changing shape dynamically and has

an unsupervised training nature. Meanwhile, strain data obtained in contact method can also be related to displacements via neural network model, as Bruno, R., et al. did in JPL. [26]

Besides artificial neural network, other relationship was established based on physical modeling. Foss, G.C. et al. first suggested the concept of a modal transformation algorithm to reproduce deformations from strains and a structure's modal characteristics. Experiment on a simply supported plate was implemented to validate the approach. [27][29] P. Bogert solved this inverse problem through modal transformation, which uses the structure's deformation and strain modes, in conjunction with the discrete strain data, to determine the deformed shape. [27] Bernasconi and Ewins demonstrated determination of mass-normalized modal strain fields from strain gages. [27][30]

Similar types of algorithms can be considered in non-contact sensing regime, Audette, M.A., et al. present a literature survey on the algorithms of automatic surface registration techniques, and various approaches were covered for each of the partitioned steps: choice of transformation, elaboration of surface representation and similarity criterion, and matching and global optimization; especially in the issue of surface representation, approaches based on feature, cloud of points, global shape and physical model were reviewed. [31]

As a summary, the algorithm of data integration is a fast and straight-forward approach to get displacement determination, if the structure is simple in spatial domain. For a complicated structure, especially space aperture, it is more necessary to enhance the performance of algorithms in order to compensate the incomplete onboard measurements. Physical model or data-based neural network model will be adopted, and as a result, more of the quality of shape reconstruction will depend on the on-ground or off-line, such as system straining and mechanism development. [26]

2.2. Candidate Approaches

Given a series of distributed strain measurements from a fiber Bragg grating array, the major subsequent objective is to reconstruct the global shape of a 3-D large, flexible structure according to that sensing architecture. Due to cost consideration, usually the number of sensors is limited, which necessitates

optimization of the structural sensing architecture. The data analysis methodology also plays an important role for enhancing the reconstruction accuracy. In this work, we want to study and compare two different strategies of reconstruction: simplified neural network approach and mechanics/modal basis functions approach.

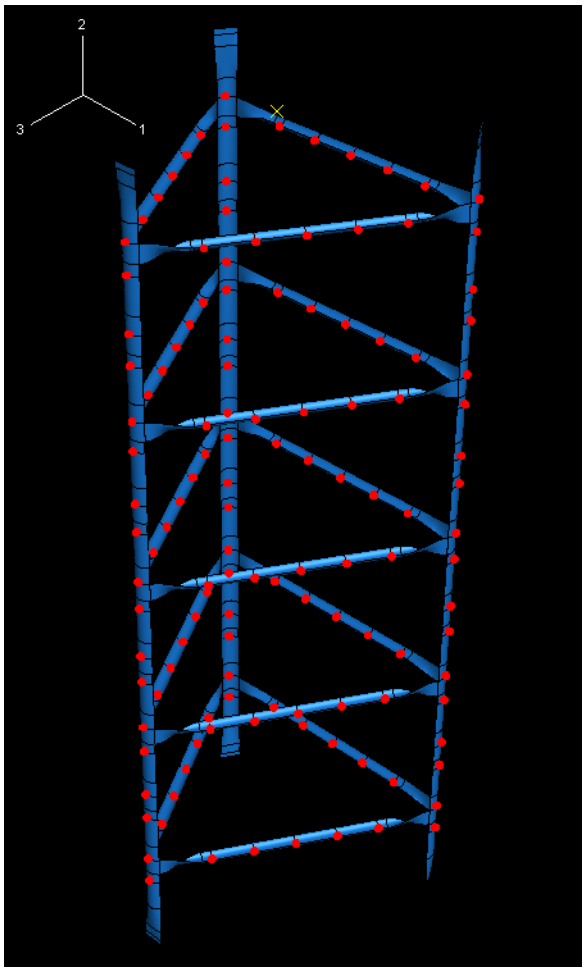

Figure 5: assembled truss with full set of interest points (IPs)

We use a finite element model based in ABAQUS, which is a widely used simulation tool, to obtain the strain and displacement data of the boom similar to what is shown in Figure 2. The flow overview is illustrated in Figure 6. The strain data generated by ABAQUS at the all interest points (IPs), shown in Figure 5, is the input of the shape reconstruction process, while the displacement data produced by ABAQUS serves as a benchmark to evaluate the accuracy of the estimated displacement from our shape reconstruction.

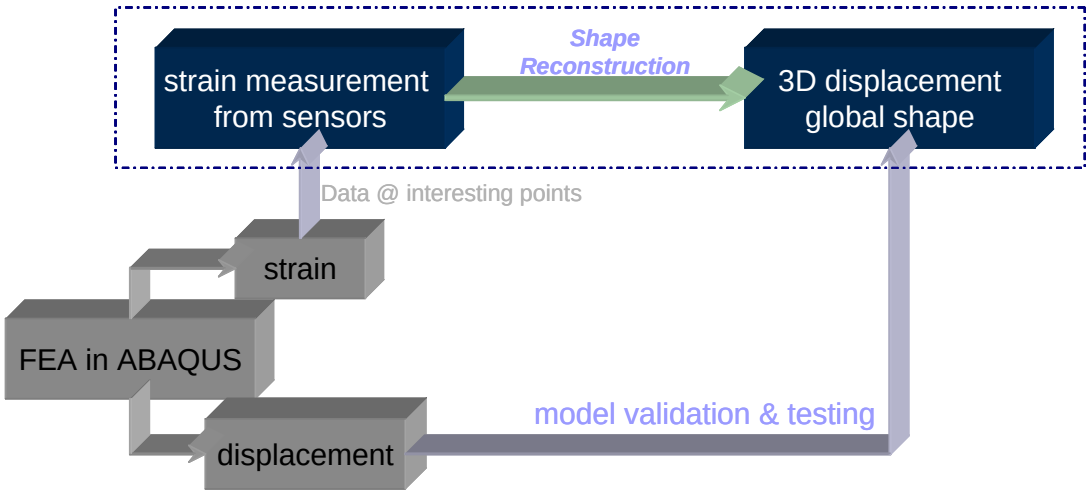

Figure 6: flow overview

Two different strategies are studied and compared in our work to reconstruct structural shape from limited strain information.

The two strategies are shown in Figure 7. The upper branch depicts the linear neural net approach, which relates the strain measurements with displacement by a simplified linear mapping. The mapping is obtained after training the system with a supervised learning mode.

The lower branch represents the idea of mechanics approach, which is based on basis function projections. This approach follows the idea that all the deformation quantities such as strains and displacements are linear combination of different functions; therefore the strain measurements and structural shapes are connected by the weighting.

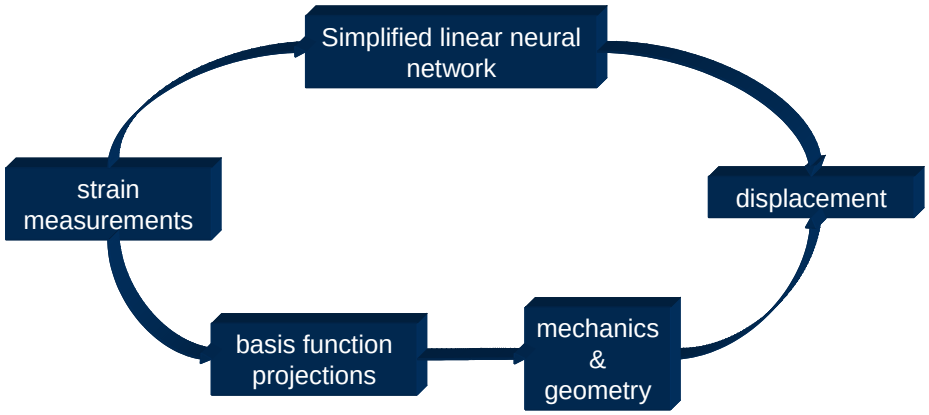

Figure 7: two different strategies in our work

2.2.1. “Linear” Neural Net: Matrix Mapping

A neural network is a general map between inputs and outputs that requires training for proper classification, and we hypothesize that, since strain-to-displacement is linear, we could form a simpler “linear neural net” between inputs (strain) and outputs (displacement configuration).

Under the assumption of linear mapping relationship between strain and displacement, a generalized neural network relationship for a single layer reduces to

$$\mathbf{U}_{3n} = \mathbf{B} \times \mathbf{E}_{n} \tag{1}$$

where **U** is the displacement vector of n IPs, with first n elements being displacement in direction 1 (see Figure 5), second n elements in direction 2, and third n elements in direction 3, and **E** is the strain vector of the n IPs, and **B** is the mapping matrix. The number of elements of **B** is $3n^2$. For a certain loading case, there are 3n equations, which are not sufficient for uniquely determine all the elements in **B**. To solve **B** accurately, we add various training cases to the structure, and Eq. (1) can be rewritten as

$$\mathbf{U}_{3n\times m} = \mathbf{B} \times \mathbf{E}_{n\times m} \tag{2}$$

where m is the number of training cases. Each column of matrix **U** corresponds to one unique training case and so does matrix **E**. The dimension of transformation matrix **B** is only determined by number of interest points, and number of training cases independent.

Eq. (3) and (4) are the expansion of Eq. (2), where **u**, **v** and **w** represent the displacements in direction 1, 2 and 3 respectively.

To solve the over-constrained system in Eq. (2), we use pseudo-inverse algorithm to determine matrix **B**, which guarantees to have the least square error. The whole process is shown in Figure 8.

$$\begin{bmatrix} \mathbf{u} \\ \mathbf{v} \\ \mathbf{w} \end{bmatrix}_{3n\times m} = \mathbf{B} \times \left[\boldsymbol{\varepsilon}\right]_{n\times m} \tag{3}$$

$$\begin{bmatrix} u_{11} & u_{12} & \cdots & u_{1m} \\ u_{21} & u_{22} & \cdots & u_{2m} \\ \vdots & \vdots & \ddots & \vdots \\ u_{n1} & u_{n2} & \cdots & u_{nm} \\ v_{11} & v_{12} & \cdots & v_{1m} \\ v_{21} & v_{22} & \cdots & v_{2m} \\ \vdots & \vdots & \ddots & \vdots \\ v_{n1} & v_{n2} & \cdots & v_{nm} \\ w_{11} & w_{12} & \cdots & w_{1m} \\ w_{21} & w_{22} & \cdots & w_{2m} \\ \vdots & \vdots & \ddots & \vdots \\ w_{n1} & w_{n2} & \cdots & w_{nm} \end{bmatrix}_{3n\times m} = \mathbf{B}_{3n\times n} \times \begin{bmatrix} \varepsilon_{11} & \varepsilon_{12} & \cdots & \varepsilon_{1m} \\ \varepsilon_{21} & \varepsilon_{22} & \cdots & \varepsilon_{2m} \\ \vdots & \vdots & \ddots & \vdots \\ \varepsilon_{n1} & \varepsilon_{n2} & \cdots & \varepsilon_{nm} \end{bmatrix}_{n\times m} \tag{4}$$

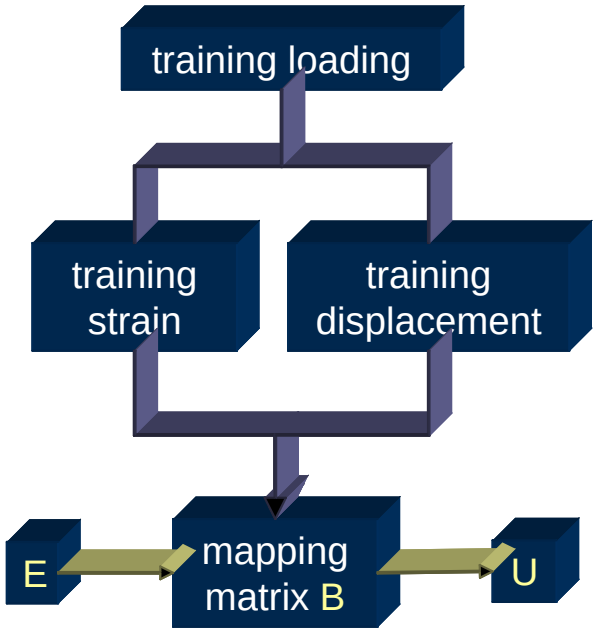

Figure 8: flow chart of matrix approach

Since the full set of IPs has been demonstrated in Figure 5, we illustrate only the locations of training cases as follows. Figure 9 shows all possible loading points in ABAQUS model, which are presented by yellow dots, and the red dots along central axes are the loading points actually selected in our training experiments.

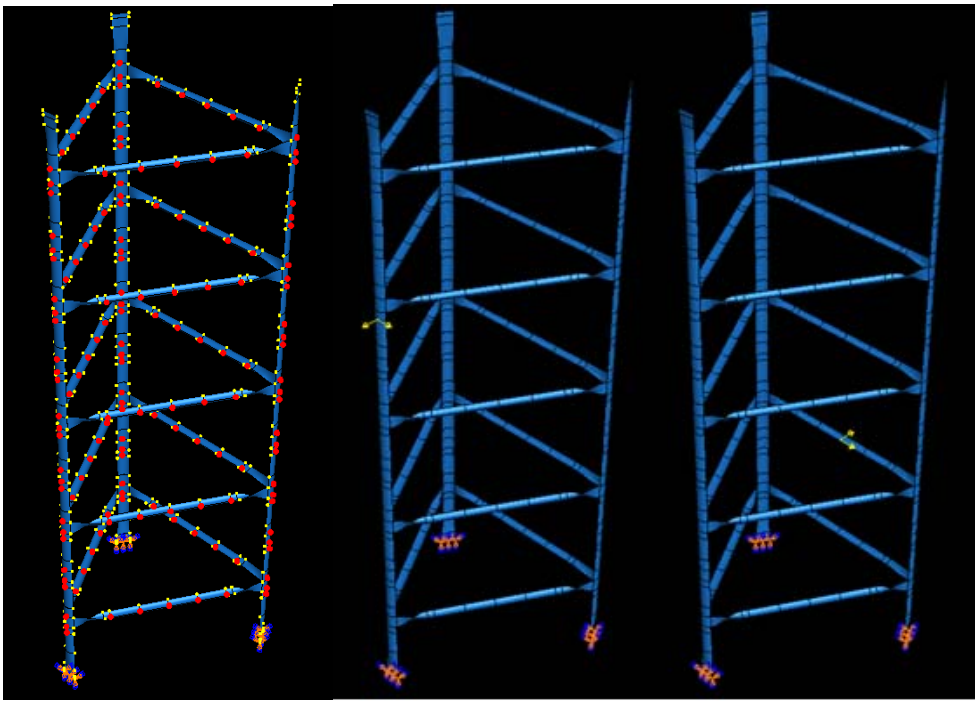

Figure 9: loading illustration

There are several issues for selecting the training points and setting up the training experiments:

1. The finally selected training points should contain all IPs that appear in the linear mapping equations.

2. Since the three longerons carry more global shape information of the structure, more training points should be located on longerons compared to battens. In our settings, there are 276 total training cases, in which 186 are located on longerons and 90 are located on battens.

3. In order to maintain the matrix **B** at full rank, we want to minimize the linear dependencies among different training cases.

4. To avoid local stress concentration, which gives us little global shape information, we choose training points on center axes of each component away from key connections that often create stress concentrations.

2.2.2. Mechanics Approach: Modal Basis Functions

The idea of mechanics approach is to decompose the deformation of an arbitrary loading to a linear combination of a set of basis functions or vectors. The coefficients of the linear combination, also we call them weighting ratios, are the same for both strain and displacement decomposition, and therefore are essential for the description of the deformation.

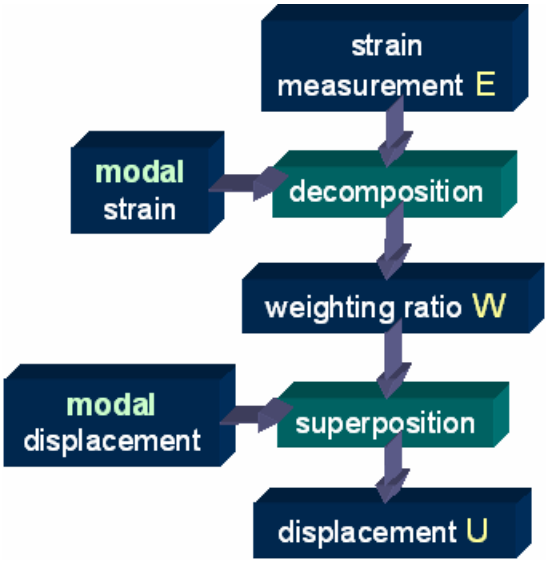

Figure 10: flow chart of modal approach

Since modal expansion technique has been widely used in dynamic analysis, we naturally choose modal functions as the set of basis to decompose the strain measurements. The main flow of this approach is given in Figure 10.

For each test loading we do the following three steps:

Step 1: we do ABAQUS finite element simulation to have the measured strain vector $\mathbf{E}^{[t]}$ in an arbitrary test, and a set of modal strains $\mathbf{E}^{[m]}$. $\mathbf{E}^{[t]}$ is an n-point vector, where n is the number of IPs. $\mathbf{E}^{[m]}$ is a matrix in which each column is a modal strain series. Due to the computation limit, we only include the first 29 modes from ABAQUS in all the following experiments. By adopting the pseudo-inverse operation in *Matlab*, we can derive the weighting of each mode, as shown in Eq. (7), Eq. (8), and Eq. (9).

$$\mathbf{E}^{[t]} = \mathbf{E}^{[m]} \times \mathbf{W} \tag{7}$$

$$\begin{bmatrix} \varepsilon_1^{[t]} \\ \varepsilon_2^{[t]} \\ \vdots \\ \varepsilon_n^{[t]} \end{bmatrix}_{n\times 1} = \begin{bmatrix} \varepsilon_1^{[m1]} & \varepsilon_1^{[m2]} & \cdots & \varepsilon_1^{[m29]} \\ \varepsilon_2^{[m1]} & \varepsilon_2^{[m2]} & \cdots & \varepsilon_2^{[m29]} \\ \vdots & \vdots & \ddots & \vdots \\ \varepsilon_n^{[m1]} & \varepsilon_n^{[m2]} & \cdots & \varepsilon_n^{[m29]} \end{bmatrix}_{n\times 29} \times \mathbf{W}_{29\times 1} \tag{8}$$

$$\mathbf{W} = (\mathbf{E}^{[m]})^{-1} \times \mathbf{E}^{[t]} \tag{9}$$

Step 2: also from ABAQUS calculation, we have the modal displacements of 3 directions on a large amount of discrete measuring points, then we use linear regression algorithm to do curve fitting with polynomial model so that the continuous displacement functions in spatial domain are obtained, as shown in Eq. (10) and Figure 11. Validation of the polynomial function is also performed.

$$\mathbf{U}_{function}^{[m]} = Polynomial\left(\mathbf{U}^{[m]}\right) \tag{10}$$

Figure 11: flow chart of modal displacement functions fitting

Step 3: we multiply the modal displacement functions by the weighting ratios derived in step 1 to produce estimated continuous displacements (shown in Eq. (11)). Alternatively, we can also multiply the modal displacement vectors by the weighting ratio, and produce estimated displacements only at IPs (shown in Eq (12), and Eq. (13)). The second method avoids the error generated in step 2, but loses a global view of 3-D motions.

$$\mathbf{U}_{function}^{[t]} = \mathbf{U}_{function}^{[m]} \times \mathbf{W} \tag{11}$$

$$\mathbf{U}^{[t]} = \mathbf{U}^{[m]} \times \mathbf{W} \tag{12}$$

$$\begin{bmatrix} u_1^{[t]} \\ u_2^{[t]} \\ \vdots \\ u_n^{[t]} \\ v_1^{[t]} \\ v_2^{[t]} \\ \vdots \\ v_n^{[t]} \\ w_1^{[t]} \\ w_2^{[t]} \\ \vdots \\ w_n^{[t]} \end{bmatrix}_{3n\times 1} = \begin{bmatrix} u_1^{[m1]} & u_1^{[m2]} & \cdots & u_1^{[m29]} \\ u_2^{[m1]} & u_2^{[m2]} & \cdots & u_2^{[m29]} \\ \vdots & \vdots & \ddots & \vdots \\ u_n^{[m1]} & u_n^{[m2]} & \cdots & u_n^{[m29]} \\ v_1^{[m1]} & v_1^{[m2]} & \cdots & v_1^{[m29]} \\ v_2^{[m1]} & v_2^{[m2]} & \cdots & v_2^{[m29]} \\ \vdots & \vdots & \ddots & \vdots \\ v_n^{[m1]} & v_n^{[m2]} & \cdots & v_n^{[m29]} \\ w_1^{[m1]} & w_1^{[m2]} & \cdots & w_1^{[m29]} \\ w_2^{[m1]} & w_2^{[m2]} & \cdots & w_2^{[m29]} \\ \vdots & \vdots & \ddots & \vdots \\ w_n^{[m1]} & w_n^{[m2]} & \cdots & w_n^{[m29]} \end{bmatrix}_{3n\times 29} \times \mathbf{W}_{29\times 1} \tag{13}$$

To evaluate the estimation accuracy, we compare the results from Eq. (11) in step 3 with the measured displacement of ABAQUS, and calculate the errors.

3. Implementation and Results

3.1. Matrix Mapping Results

3.1.1. Reconstruction test

With the transform matrix derived from the 276 training cases, we are able to approximately reconstruct the structural shape for arbitrary loading situations.

To systematically inspect the validation of the transform matrix, we need a set of tests that represents different types of possible loadings. We create 26 tests with various loadings including concentrated force, displacement specification, body force, and surface pressure (as shown in Figure 12).

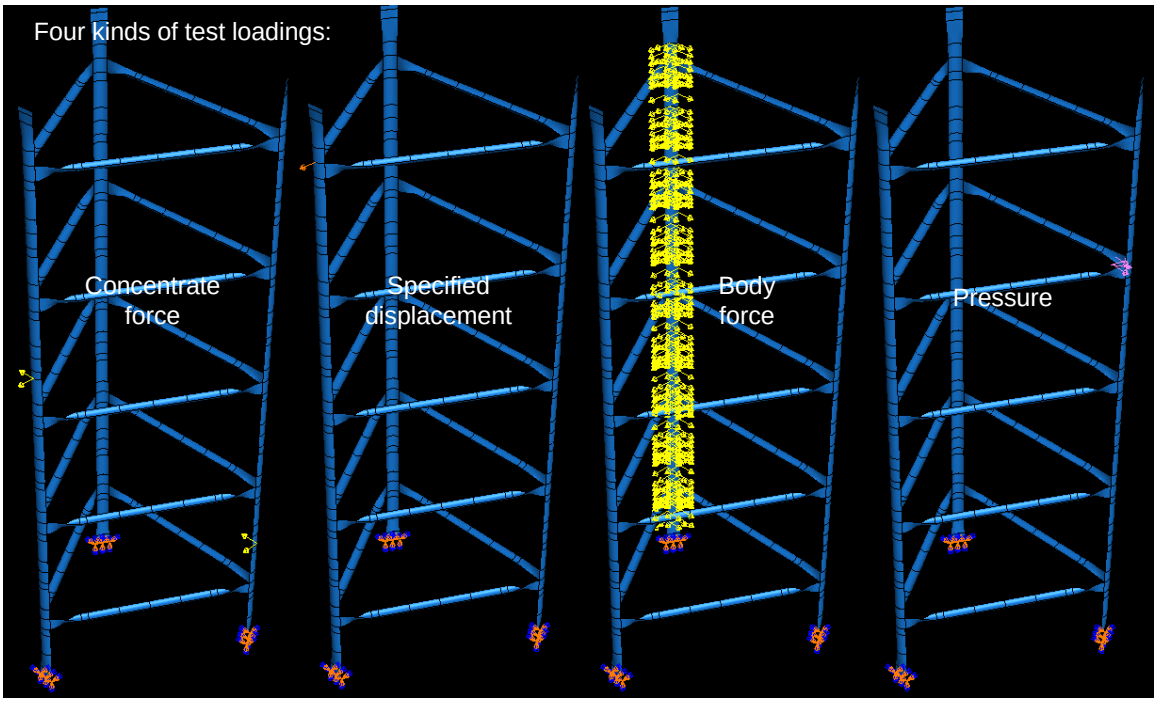

Figure 12: four types of test loadings

A quantitative criterion is necessary to evaluate the accuracy of reconstruction results for each spatial direction, and we define it in Eq. (5).

$$e^{(i)} = \sqrt{\frac{1}{n}\cdot\sum_{1}^{n}\left[\left(\frac{(\mathbf{U}^{(i)}{}_{estimation} - \mathbf{U}^{(i)}{}_{ABAQUS})}{\max(\mathbf{U}^{(1)}_{ABAQUS}, \mathbf{U}^{(2)}_{ABAQUS}, \mathbf{U}^{(3)}_{ABAQUS})}\right)^2\right]}$$

$$= \sqrt{\frac{1}{n}\cdot\sum_{1}^{n}\left[\left(\frac{(\mathbf{B}^{(i)}\times\mathbf{E}_{n\times 1} - \mathbf{U}^{(i)}{}_{ABAQUS})}{\max(\mathbf{U}^{(1)}_{ABAQUS}, \mathbf{U}^{(2)}_{ABAQUS}, \mathbf{U}^{(3)}_{ABAQUS})}\right)^2\right]} \quad (5)$$

$$i = 1,2,3 \quad \mathbf{U}^{(i)} \Leftrightarrow \mathbf{u}, \mathbf{v}, \mathbf{w}$$

The superscript is the direction index, the subscript indicates either estimation results or ABAQUS results, and n is the number of IPs. Difference of ($\mathbf{U}_{estimation} - \mathbf{U}_{ABAQUS}$) for a certain "n" and a direction "i" is the absolute error, and is normalized when divided by the maximal displacement of the structure along any direction.

Three factors influence the error defined in Eq. (5): number of training cases, number of IPs and locations of IPs. We will discuss their effects respectively in the following sections.

3.1.2. Parameter study

In this section, the three factors that affect the reconstruction error will be studied, number of training cases, number of interest points and locations of interest points.

Number of training cases:

To analyze the effect of number of training cases upon reconstruction accuracy, we firstly randomly choose N_c cases from the total 276 cases to train the system, and then validate the system with 26 test cases. The normalized RMS errors of the 26 test cases are averaged and then compared for N_c=120, 180, 240, and 276. All 129 IPs are used in this experiment. The relationship between N_c and the average error are shown in Figure 13, in which the trend is very obvious that more training cases increases the accuracy. Meanwhile, it is noticeable that shape sensing fails when number N_c is too small, such as N_c=120.

The average error in Figure 11 is defined in Eq. (6), where the "$e^{(i)}$" has been defined in Eq. (5).

$$\bar{e} = \frac{1}{26} \cdot \sum_{test=1}^{26} \left(\sum_{i=1}^{3} \mathbf{e}_{test}^{(i)} \right) \tag{6}$$

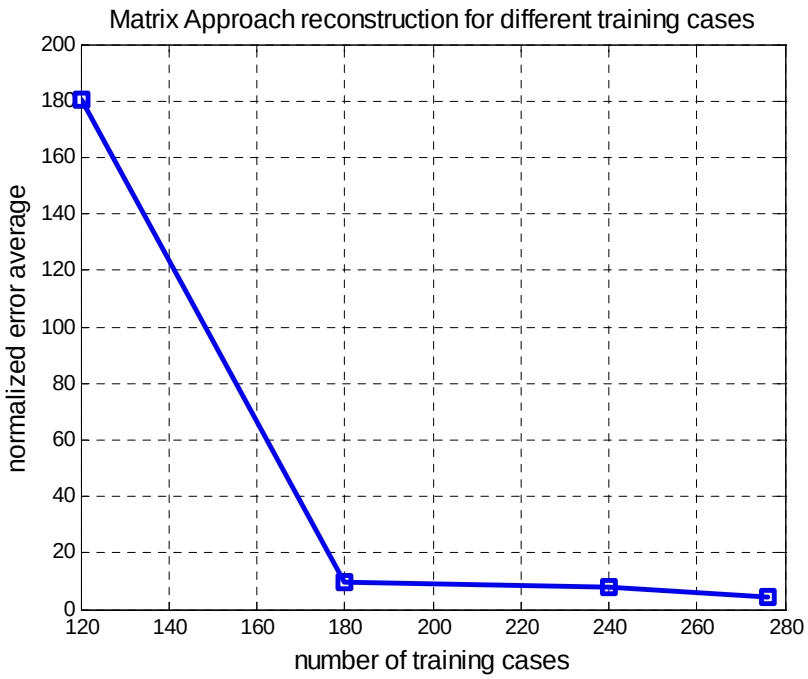

Figure 13: matrix approach reconstruction for different training cases

We notice that the consistency between the type of training cases and the type of test cases also has effect on the reconstruction accuracy. When we test the system with concentrated forces, the error becomes smaller since the system has been trained with cases of concentrated forces.

Table 3 shows the detailed results of N_c=276, full set of trainings we did. It includes the total error and the errors along direction 1, 2 and 3, (**u**, **v** and **w** in the table), with different test cases. The first column gives the type of test loading, in which "c" indicates concentrated force, "d" means displacement specification, "p" represents surface pressure, and "b" is body force. The second column shows the case indices. Column 3, 4, and 5 give the displacement components of **u**, **v** and **w** for Longeron 1, and similarly, column 6, 7, and 8 and 9, 10, and 11 are for Longeron 2 and Longeron 3 respectively. We show the values

of displacement in direction 2 (**v** component) with milli unit due to its small magnitude. The rightmost column gives the summation of error values in each row.

Table 3: detailed results of shape sensing errors

matrix approach / 276 trainings / 129IPs											
Desc.	#	**Longeron_1**			**Longeron_2**			**Longeron_3**			**Σ**
		u	**v** / 1e-003	**w**	**u**	**v** / 1e-003	**w**	**u**	**v** / 1e-003	**w**	
c	1	0.4357	2.1460	0.4088	0.1450	1.8780	0.6762	0.0965	0.6881	0.1547	1.9216
c	2	0.0325	0.2076	0.0151	0.0771	0.2902	0.0554	0.0795	0.4461	0.0682	0.3287
c	3	0.4357	2.1460	0.4088	0.1450	1.8780	0.6762	0.0965	0.6881	0.1547	1.9216
c	4	0.0042	0.0380	0.0073	0.0209	0.0715	0.0223	0.0178	0.0912	0.0027	0.0754
c	5	0.0633	2.9930	0.2548	0.4259	2.4144	0.2213	0.4550	1.9245	0.5580	1.9856
c	6	0.1340	0.7414	0.0612	0.1022	0.3410	0.1007	0.1136	0.3064	0.1649	0.6780
d	7	8.9505	30.1726	1.2806	4.7861	29.6619	0.4611	4.0796	41.6966	2.0971	21.7565
d	8	0.7317	5.7149	0.8896	0.9183	10.6673	1.6246	0.9208	6.0897	0.4685	5.5760
d	9	0.0514	0.5362	0.0741	0.2932	1.5457	0.0506	0.2958	1.0727	0.2085	0.9768
d	10	0.0156	0.5722	0.0856	0.3116	1.0744	0.2673	0.3002	1.6017	0.0859	1.0694
p	11	1.3052	12.2174	1.9810	1.2086	7.5408	2.5721	1.1561	9.7286	1.0064	9.2589
p	12	0.2759	0.3313	0.0409	0.2963	0.9974	0.2654	0.2801	0.8115	0.2967	1.4574
p	13	5.6743	29.4113	4.0544	4.9708	33.2858	0.5600	5.9631	15.1011	10.2066	31.5070
p	14	0.0555	1.1127	0.1572	0.5058	2.6227	0.1378	0.4796	1.6357	0.4073	1.7486
b	15	0.8920	10.7736	1.5771	1.2636	5.6451	2.0282	1.2532	9.1758	0.7035	7.7432
b	16	0.1509	0.1808	0.0177	0.2173	0.5627	0.2392	0.2075	0.7331	0.1923	1.0264
b	17	0.1351	0.7987	0.1287	0.2595	1.6590	0.0276	0.2691	0.8871	0.3039	1.1272
b	18	1.7379	2.6033	0.6154	1.2280	7.4155	0.2428	1.1764	9.7310	1.1416	6.1618
b	19	0.1968	0.3594	0.0829	0.1111	0.2589	0.1111	0.1094	0.3876	0.2846	0.8969
b	20	0.3194	0.1840	0.0318	0.1326	0.1921	0.2925	0.1302	0.0334	0.2294	1.1363
b	21	0.2788	0.8073	0.1222	0.1027	0.2802	0.1036	0.0938	1.0929	0.1883	0.8916
b	22	1.3662	2.1110	0.1095	1.4692	7.8203	0.2744	1.4030	5.9644	0.3665	5.0047
b	23	0.1946	0.3226	0.0524	0.1847	0.6038	0.1660	0.1722	0.3356	0.2550	1.0262
b	24	1.2183	2.9346	0.7634	0.8127	5.1316	0.1805	0.4691	6.9693	1.5496	5.0086
b	25	0.0904	0.0718	0.0177	0.3083	1.3647	0.1439	0.3004	1.4430	0.1030	0.9666
b	26	0.5623	0.4526	0.0347	0.7219	4.1839	0.1984	0.8116	4.2114	0.1849	2.5226
average		**0.9734**	**4.2285**	**0.5105**	**0.8084**	**4.9764**	**0.4500**	**0.7973**	**4.7249**	**0.8224**	***4.3759***

We can have the following observations from the experimental results in this section:

1. Generally, reconstruction accuracy increases when the number of training cases grows.

2. When the number of training cases is too small, the shape sensing fails.

3. The consistency between the type of training cases and the type of test cases is beneficial to the reconstruction accuracy. It is thus important when training the model (or the actual specimen) that the training load cases span what is expected in reality to the degree possible; such a linear matrix mapping has a reduced extrapolation window that perhaps a nonlinear mapping would not have.

Number of interest points:

To analyze the effect of number of IPs, we use 276 training cases and select uniform distribution of IPs (i.e. identical selection of points for each batten and longeron.), but vary the total number of IPs alone.

There are five IPs on each batten unit, which is denoted as [1 2 3 4 5] (shown in Figure 14-a), and two IPs on each longeron unit, denoted as [1 2] (shown in Figure 14-b). The total structure contains five floors, each floor has three batten units, and a longeron has nine units. If we pick IPs uniformly, a subset of array [1 2 3 4 5] for batten unit with a subset of array [1 2] for longeron unit generate a global IP distribution.

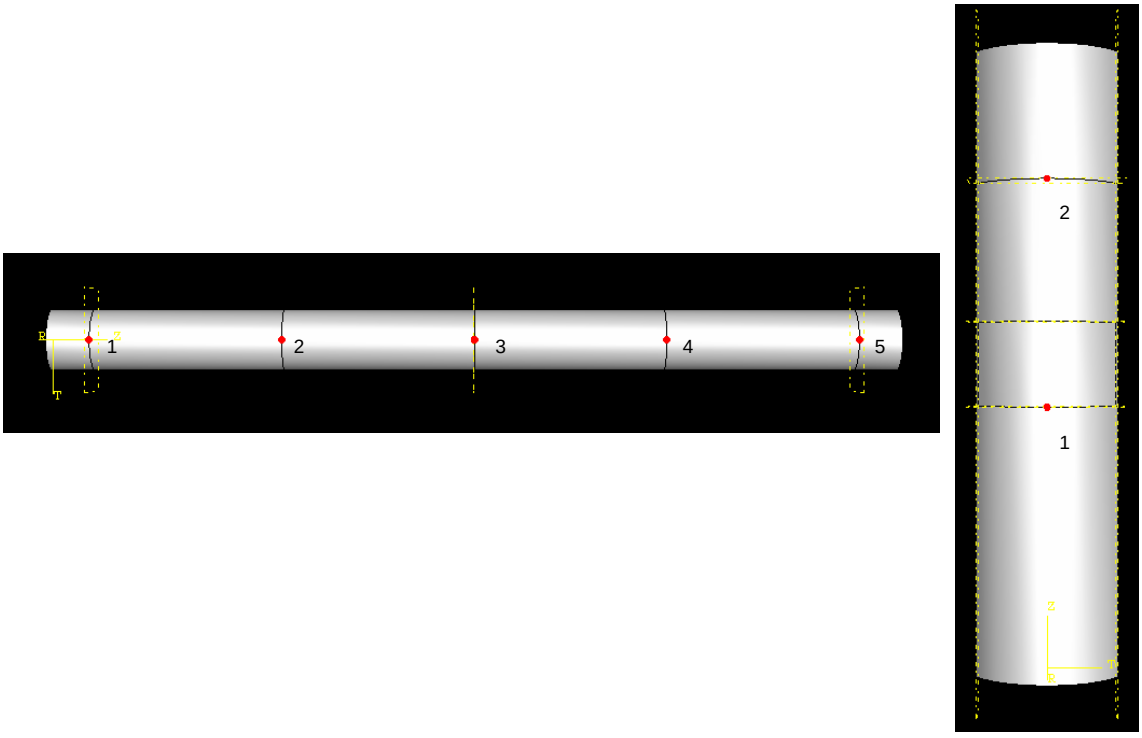

Figure 14: IP labels on batten unit (left, Fig. 14-a) and longeron unit (right, Fig. 14-b)

We vary the number of IPs from 54 to 129, and the corresponded normalized RMS error averages are given in Figure 15. The global views of different IPs selections are also depicted in the zoom-in region for errors less than 15.

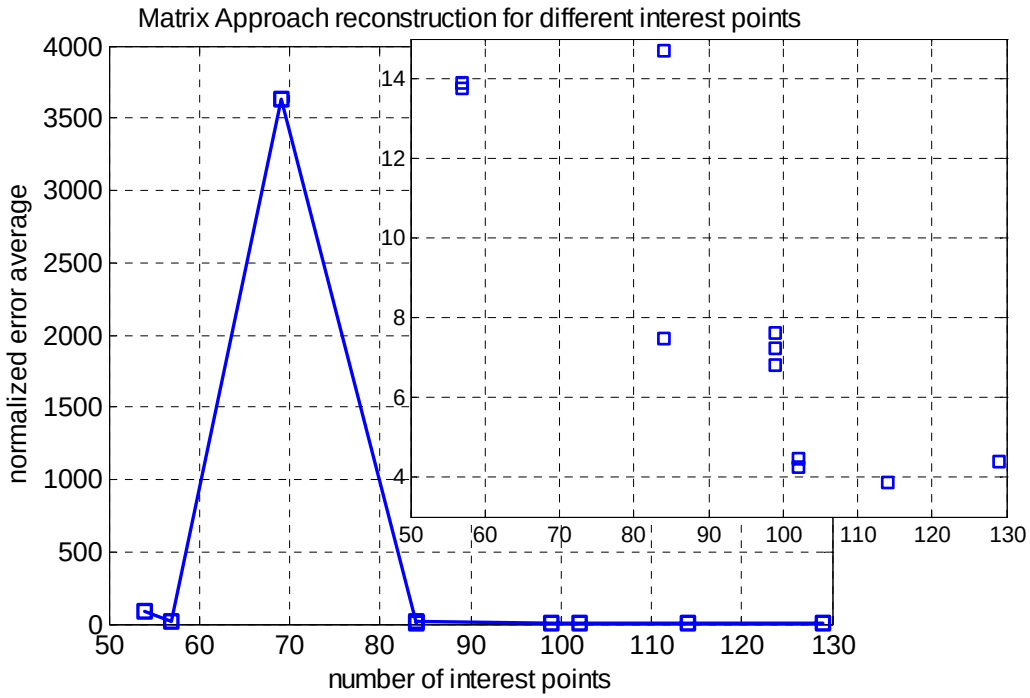

Figure 15: matrix approach reconstruction for different interest points

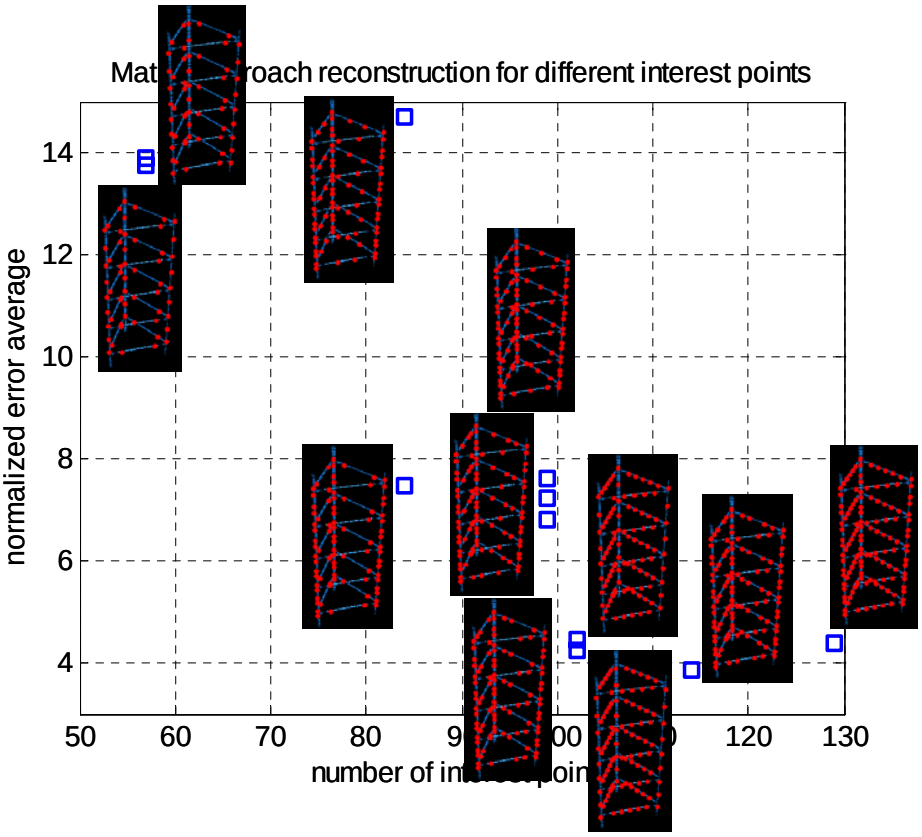

Figure 16: zooming in of Figure 15 with global views of different IPs selections

Three observations from the experimental results can be concluded as follows:

1. Similar with the effect of number of training cases, when more IPs are included, the total error drops to a tolerable level.

2. When the number of IPs is too small, the shape reconstruction fails.

3. When the number of IPs is adequately high, for example larger than 80, the correlation between average error and the number of IPs are not strong.

Table 4 gives detailed results when the subsets [1 2 4 5] for unit battens and the subsets [1 2] for unit longerons are chosen. The table format follows Table 3.

Table 4: detailed results of shape sensing errors

matrix approach / 276 trainings / IP 1 2 4 5& 1:2/ 114											
Desc.	#	**Longeron_1**			**Longeron_2**			**Longeron_3**			**Σ**
		u	**v** / 1e-003	**w**	**u**	**v** / 1e-003	**w**	**u**	**v** / 1e-003	**w**	
c	1	0.5798	2.1008	0.3192	0.1719	1.9774	0.5428	0.1026	0.6589	0.1448	1.8658
c	2	0.0642	0.2551	0.0338	0.1037	0.3330	0.0732	0.0832	0.5910	0.0552	0.4145
c	3	0.5798	2.1008	0.3192	0.1719	1.9774	0.5428	0.1026	0.6589	0.1448	1.8658
c	**4**	**0.0034**	**0.0606**	**0.0114**	**0.0261**	**0.0543**	**0.0328**	**0.0168**	**0.1011**	**0.0066**	**0.0973**
c	5	0.2355	4.2610	0.4591	0.2800	3.1649	0.1650	0.4292	1.6989	0.9843	2.5622
c	6	0.1149	0.7243	0.0581	0.0661	0.3342	0.0576	0.0830	0.2792	0.1001	0.4811
d	7	4.3126	24.3075	1.4062	2.2205	15.8325	1.0441	2.0452	19.4318	0.9872	12.0754
d	8	1.7324	4.2617	0.6778	1.0658	12.0005	1.8802	0.9938	8.1694	0.7145	7.0889
d	9	0.0684	0.4214	0.0615	0.3023	1.5154	0.0621	0.2994	1.1268	0.1868	0.9836
d	10	0.0055	0.6899	0.0979	0.3287	1.0189	0.2986	0.3092	1.6545	0.0797	1.1230
p	11	0.6415	9.0494	1.1252	1.0620	5.6983	0.6451	0.8315	9.2761	1.4365	5.7658
p	12	0.1035	0.3648	0.0366	0.3778	1.2448	0.3125	0.3125	1.2994	0.1326	1.2784
p	13	2.3095	16.4581	2.6409	8.2489	42.2286	1.7010	6.8285	26.0264	5.9729	27.7864
p	14	0.0876	0.6163	0.0775	0.5999	2.7128	0.2404	0.5148	2.2546	0.2363	1.7621
b	15	0.8820	9.3174	0.9495	1.1965	6.1810	0.4462	1.0605	9.1819	1.1801	5.7395
b	16	0.1525	0.4778	0.0562	0.2489	0.4775	0.3036	0.2303	0.9296	0.1659	1.1593
b	17	0.0465	0.3975	0.0676	0.3403	1.7674	0.0734	0.2951	1.3237	0.1650	0.9914
b	18	2.3775	3.3762	0.7948	1.6620	8.8893	0.3646	1.4790	12.0502	1.5541	8.2563
b	19	0.2203	0.3425	0.0789	0.0963	0.2123	0.1166	0.0959	0.3815	0.2841	0.8930
b	20	0.3299	0.1582	0.0266	0.1325	0.2137	0.2952	0.1242	0.0790	0.2332	1.1421
b	21	0.2195	0.3814	0.0566	0.0505	0.3758	0.0211	0.0752	0.6664	0.0789	0.5032
b	22	1.4034	2.1575	0.1115	1.3479	7.6308	0.1713	1.2349	5.8865	0.2540	4.5387
b	23	0.1557	0.1411	0.0117	0.2202	0.5747	0.2210	0.1966	0.5938	0.2031	1.0096
b	24	2.2169	4.1887	0.9961	1.3508	7.1292	0.2609	1.0548	10.7503	1.8826	7.7842
b	25	0.1141	0.2055	0.0335	0.3253	1.3451	0.1654	0.3020	1.5319	0.0696	1.0130
b	26	0.4376	0.5421	0.0512	0.6415	3.1939	0.2464	0.6394	3.4258	0.0585	2.0818
average		**0.7459**	**3.3599**	**0.4061**	**0.8707**	**4.9263**	**0.3955**	**0.7592**	**4.6164**	**0.6658**	***3.8562***

Location of interest points:

We discuss the effect of the locations of IPs in this section, based on the same experiment in the last section. We re-summarize the results in Figure 15 and Figure 16. For simplicity, we name different combination of IPs with collection indices and put them in column 1 and 5 of Table 5. Column 2 shows the corresponding number of IPs. Column 3 and 4 are the batten/longeron IP selection patterns, and column 4 is average RMS errors.

Table 5: averaged error with different IP locations for matrix approach

Collection #	Number of total IPs	Batten IP selection	Longeron IP selection	Averaged RMS error	Collection #
1	129	[1 2 3 4 5]	[1 2]	4.3759	1
2	102	[1 2 3 4 5]	[1]	4.2327	2
3	102	[1 2 3 4 5]	[2]	4.4635	3
4	114	[1 2 4 5]	[1 2]	3.8562	4
5	99	[1 3 5]	[1 2]	7.6095	5
6	99	[1 4 5]	[1 2]	6.8239	6
7	99	[1 2 4]	[1 2]	7.2213	7
8	84	[1 5]	[1 2]	7.4825	8
9	84	[2 4]	[1 2]	14.7183	9
10	57	[1 5]	[1]	13.8869	10
11	57	[1 5]	[2]	13.7469	11
12	69	[3]	[1 2]	3,633.144	12
13	54	[ ]	[1 2]	85.6679	13

We can have the following observations:

1. In collection 1, 2 and 3, it can be seen that the error keeps fairly the same when we choose different longeron IP patterns and maintain the same batten IP patterns. Similar phenomenon appears also in collection 10 and 11. Hence, the shape reconstruction results are not sensitive to the locations of IPs on longeron.

2. In contrast to collect 1, collect 4 does not choose IP#3 in batten unit, and the error becomes smaller. Compare collection 8 to 5 and 13 to 12, we can see the similar thing.

3. Comparing collection 8 to collection 9, with the same amount of IPs, we find [1 5] is far more effective in shape sensing than [2 4]. This statement is also supported by comparing collection 6 to collection 7.

3.1.3. Reconstruction visualization

As an example with good shape reconstruction, the results of test case #4 are shown in Figure 17, Figure 18, and Figure 19. Figure 17 shows the loading for the test, and Figure 18 illustrates the deformed shape of the test. The estimated/real displacements along three different directions are shown in Figure 19.

We can see that the matrix approach can grasp the global shaping information fairly well from the strain input, with a proper training process.

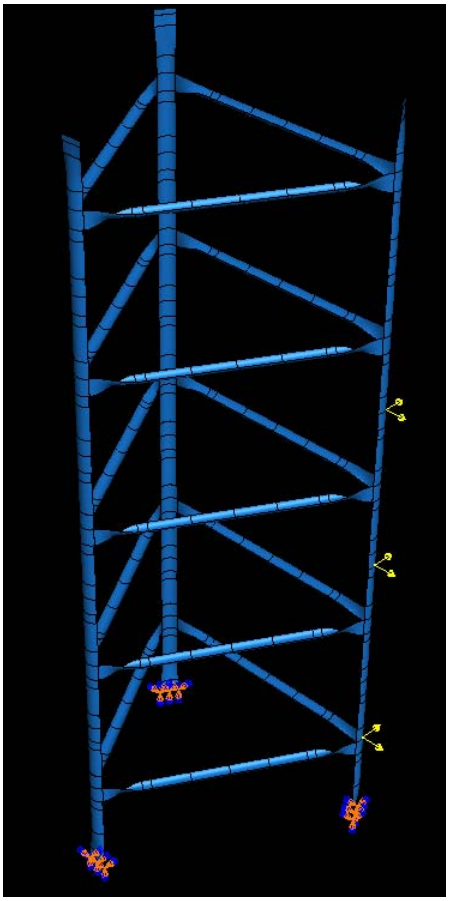

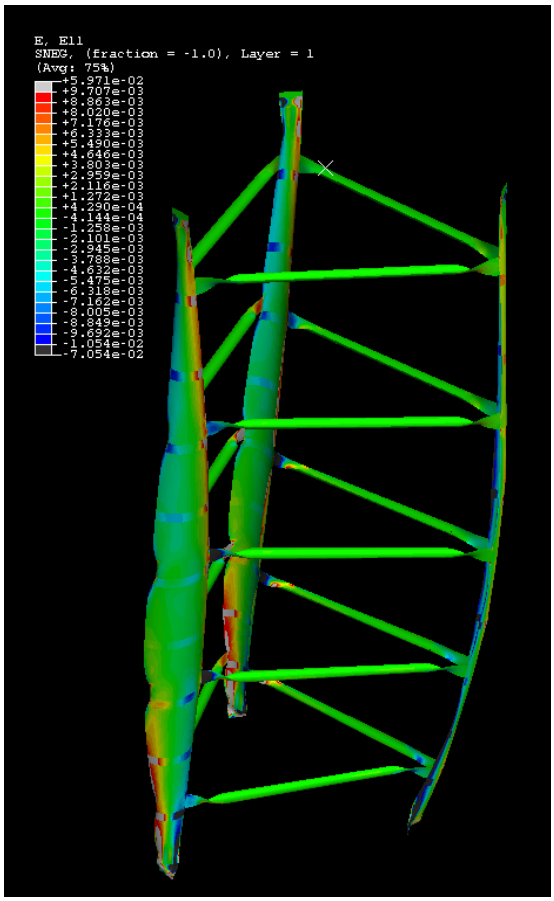

Figure 17: test case #4 loading illustration (left)

Figure 18: test case #4 deformation and strain distribution illustration (right)

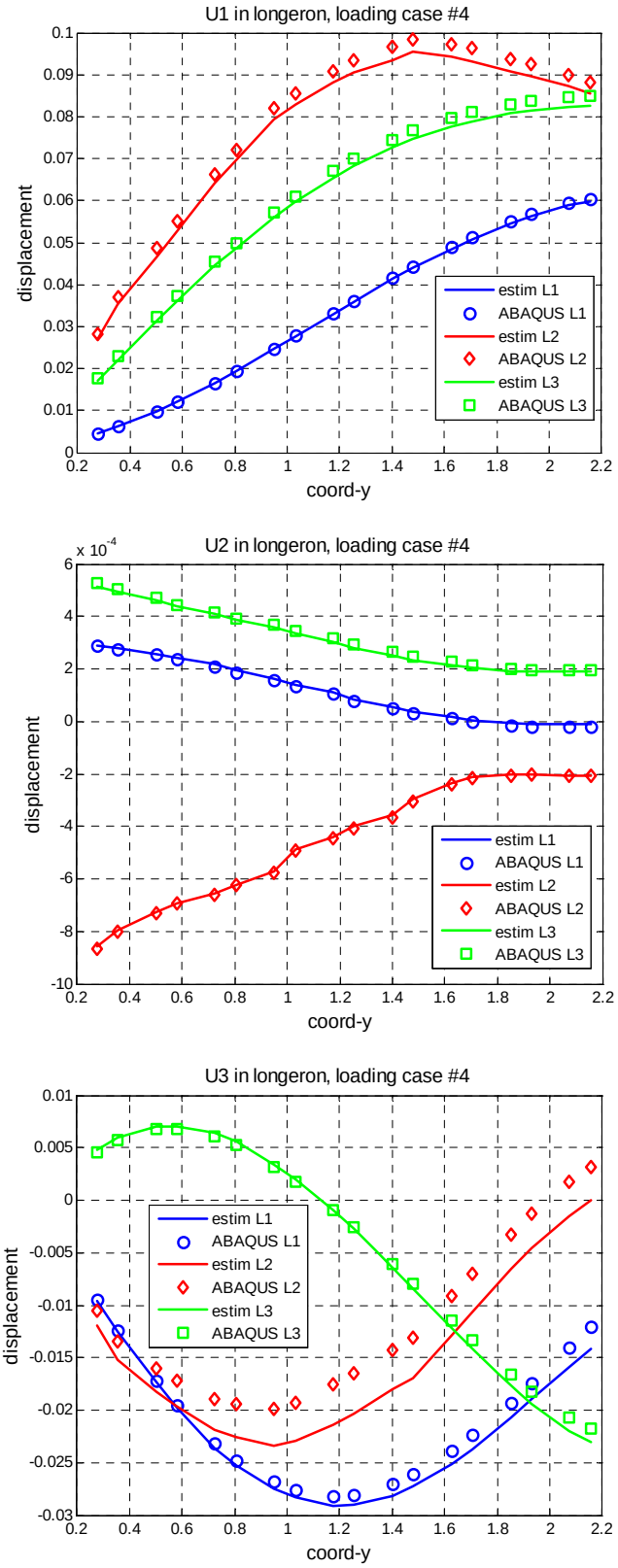

Figure 19: test case #4 displacement reconstruction curves

3.2. Modal Basis Functions Approach Results

3.2.1. Modal analysis

We perform modal analysis on the finite element model in ABAQUS to have the measured modal strain and displacement information. For completeness, we list the natural frequencies and mode shape descriptions in Table 6. Only first 29 modes are analyzed in our experiments. The pictorial representations of the first four modes are given in Figure 20 to Figure 23. The amplitudes of longitudinal strain are shown in these figures.

Table 6: first 29 natural frequencies

Mode #	1	2	3	4	5	6	7	8
Natural frequency (Hz)	10.777	10.777	17.260	19.192	19.192	30.452	32.752	32.752
description	bending	bending	torsion	bending	bending	torsion	bending	bending
Mode #	9	10	11	12	13	14	15	16
Natural frequency (Hz)	33.686	41.739	43.891	43.891	49.764	49.764	51.132	51.240
description	torsion	torsion	bending	bending	bending	bending	bending	bending
Mode #	17	18	19	20	21	22	23	24
Natural frequency (Hz)	51.597	52.310	53.258	54.450	54.450	55.481	55.481	58.919
description	bending	bending	bending	bending	bending	bending	bending	torsion
Mode #	25	26	27	28	29	30	31	32
Natural frequency (Hz)	62.837	62.837	62.964	72.026	72.026	-	-	-
description	torsion	torsion	torsion	torsion	torsion	-	-	-

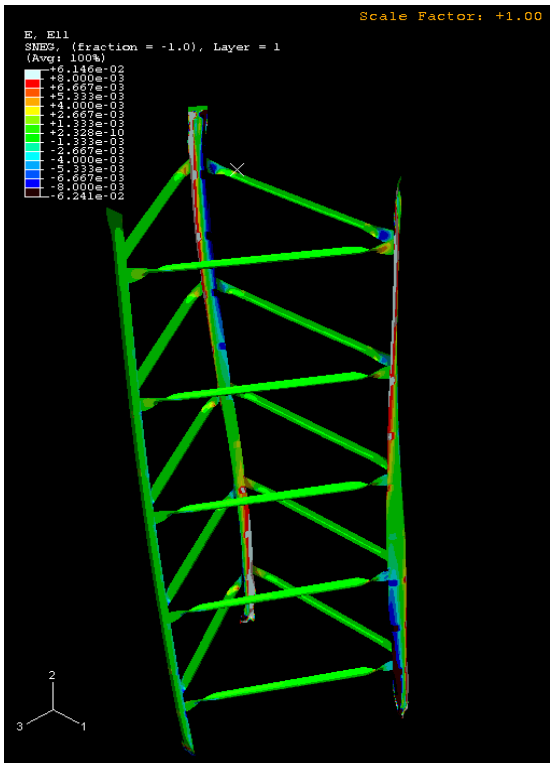

Figure 20: the first mode shape

Figure 21: the second mode shape

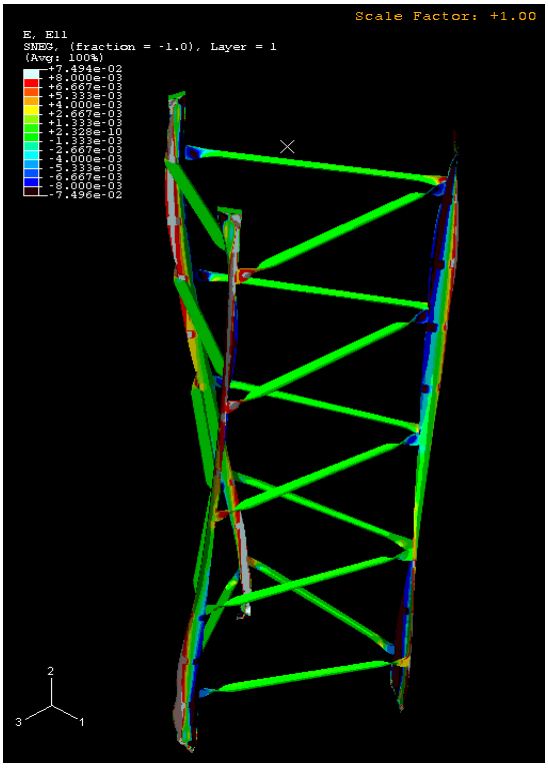

Figure 22: the third mode shape

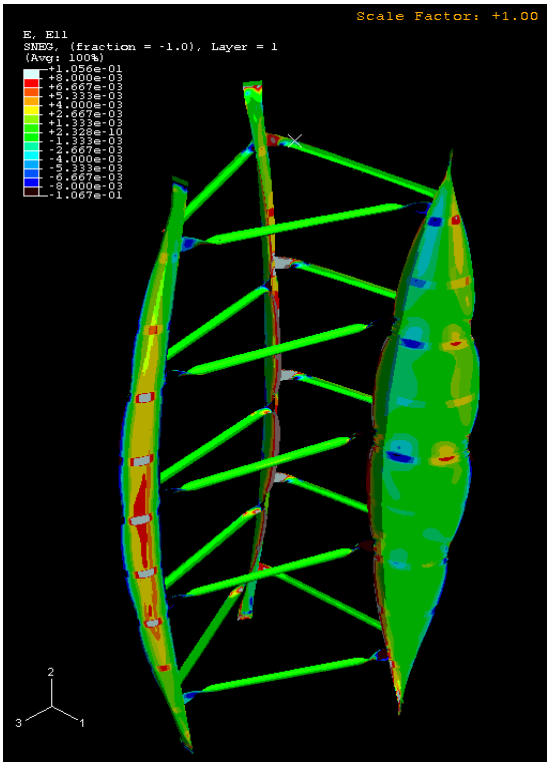

Figure 23: the fourth mode shape

3.2.2. Modal functions

We assume the polynomial model for modal displacement function has the following form:

$$\phi_x^m(x,y,z) = \sum_{i=0}^{N_x}\sum_{j=0}^{N_y}\sum_{k=0}^{N_z} a_{ijk}^m x^i y^j z^k \tag{14}$$

$$\phi_y^m(x,y,z) = \sum_{i=0}^{N_x}\sum_{j=0}^{N_y}\sum_{k=0}^{N_z} b_{ijk}^m x^i y^j z^k \tag{15}$$

$$\phi_z^m(x,y,z) = \sum_{i=0}^{N_x}\sum_{j=0}^{N_y}\sum_{k=0}^{N_z} c_{ijk}^m x^i y^j z^k \tag{16}$$

where N_x, N_y, N_z are the highest orders for coordinate variables x, y, and z (matching to direction 1, 2, and 3). $a^m_{i,j,k}$, $b^m_{i,j,k}$, and $c^m_{i,j,k}$ are the coefficients for each polynomial term, and we need to find those coefficients for all the terms in our fitting functions $\phi^m_x(x,y,z)$, $\phi^m_y(x,y,z)$, and $\phi^m_z(x,y,z)$ with linear regression algorithm.

In our application, we only concern about the longerons' movements, and the highest order for x and z term is zero, so the polynomial model reduces to:

$$\phi_x^m(y) = \sum_{j=0}^{N} a_j^m y^j \tag{17}$$

$$\phi_y^m(y) = \sum_{j=0}^{N} b_j^m y^j \tag{18}$$

$$\phi_z^m(y) = \sum_{j=0}^{N} c_j^m y^j \tag{19}$$

where N is the highest polynomial order applied to the mode fitting.

The boundary conditions can be written as follows (shown in Table 7):

Table 7: boundary conditions for linear regression of modal displacement functions

$y=0$	$\phi_x^m(y)=0$	$\phi_y^m(y)=0$	$\phi_z^m(y)=0$	zero displacement
	$\frac{\partial\phi_x^m(y)}{\partial y}=0$	-	$\frac{\partial\phi_z^m(y)}{\partial y}=0$	zero slope
$y=h$	-	$\frac{\partial\phi_y^m(y)}{\partial y}=0$	-	zero axial force
	$\frac{\partial^2\phi_x^m(y)}{\partial y^2}=0$	-	$\frac{\partial^2\phi_z^m(y)}{\partial y^2}=0$	zero bending
	$\frac{\partial^3\phi_x^m(y)}{\partial y^3}=0$	-	$\frac{\partial^3\phi_z^m(y)}{\partial y^3}=0$	zero shearing

3.2.3. Order selection of the polynomial model

We try different highest polynomial order N (as in Eq. (17), Eq. (18) and Eq. (19)) from 3 to 24, tabulate and plot the summation of RMS errors for the curve fitting results in Table 8 and Figure 24. It can be noticed that the error drops when N increases, and the trend of convergences to zero is obvious. The errors of **u**, **v**, **w** along three directions are plotted with log scale from Figure 25 to Figure 27 respectively.

Table 8: detailed curving fitting results

average RMS error of displacement fitting /m										
Order: N	**longeron 1**			**longeron 2**			**longeron 3**			average
	u	**v** /1e-3	**w**	**u**	**v**/1e-3	**w**	**u**	**v**/1e-3	**w**	
3	0.1033	1.0513	0.1227	0.1406	1.1496	0.1281	0.1380	1.0494	0.1243	**0.0845**
5	0.0244	0.3947	0.0602	0.0627	0.4025	0.0447	0.0599	0.3733	0.0433	**0.0329**
8	0.0053	0.1397	0.0135	0.0134	0.1436	0.0098	0.0126	0.1341	0.0099	**0.0072**
10	0.0019	0.0914	0.0072	0.0070	0.0941	0.0047	0.0064	0.0869	0.0046	**0.0036**
12	0.0010	0.0757	0.0045	0.0043	0.0780	0.0028	0.0039	0.0718	0.0027	**0.0022**
16	0.0003	0.0508	0.0018	0.0017	0.0521	0.0011	0.0016	0.0483	0.0010	**0.0009**
18	0.0003	0.0416	0.0014	0.0013	0.0428	0.0008	0.0012	0.0399	0.0008	**0.0007**
20	0.0002	0.0369	0.0009	0.0008	0.0380	0.0006	0.0008	0.0355	0.0005	**0.0004**
24	0.0002	0.0311	0.0006	0.0006	0.0323	0.0004	0.0006	0.0300	0.0004	**0.0003**

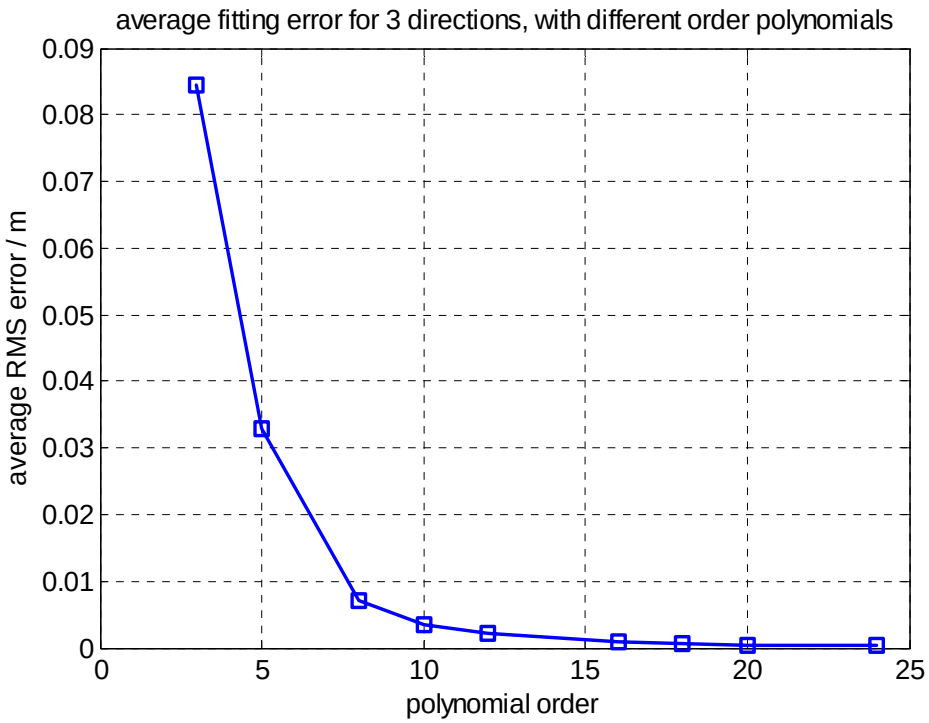

Figure 24: total fitting error with different orders of polynomial model

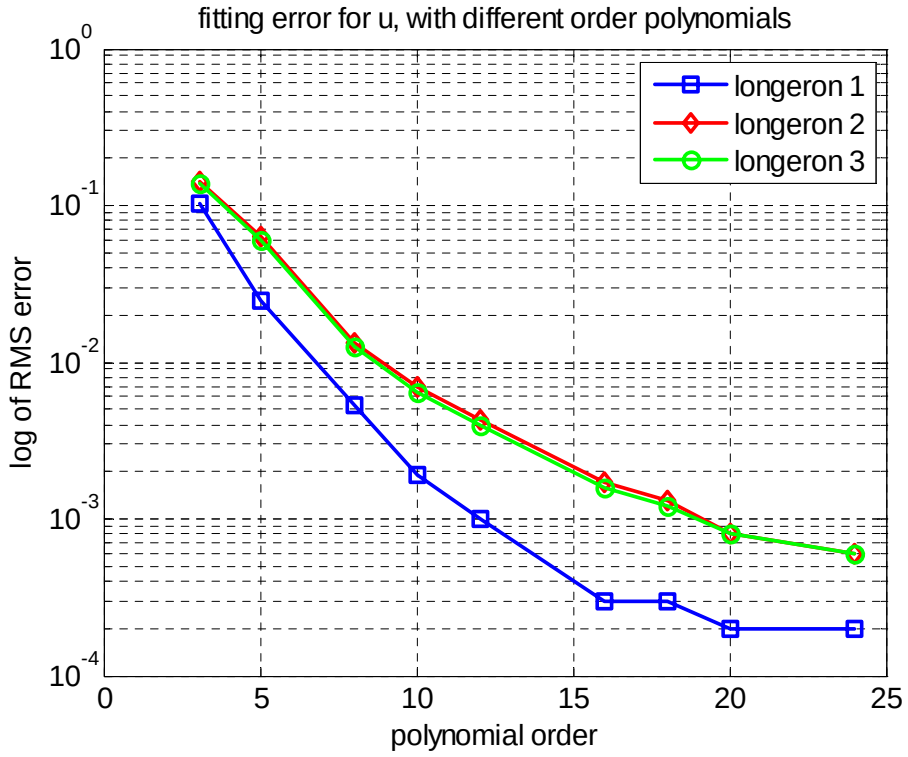

Figure 25: fitting error of “u” in log scale, with different orders of polynomial model

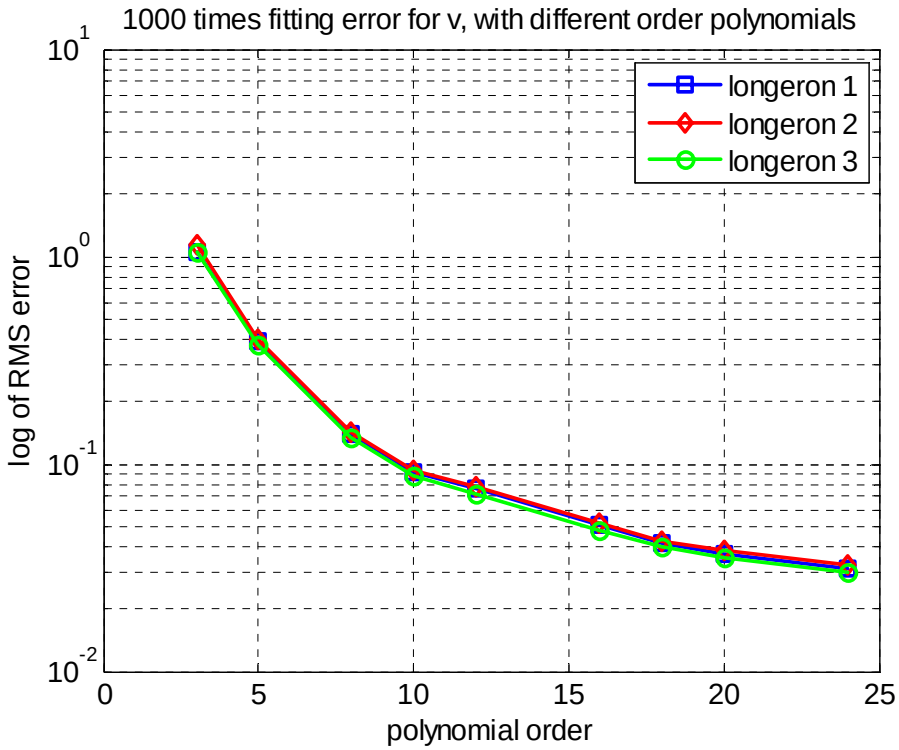

Figure 26: fitting error of "v" in log scale, with different orders of polynomial model

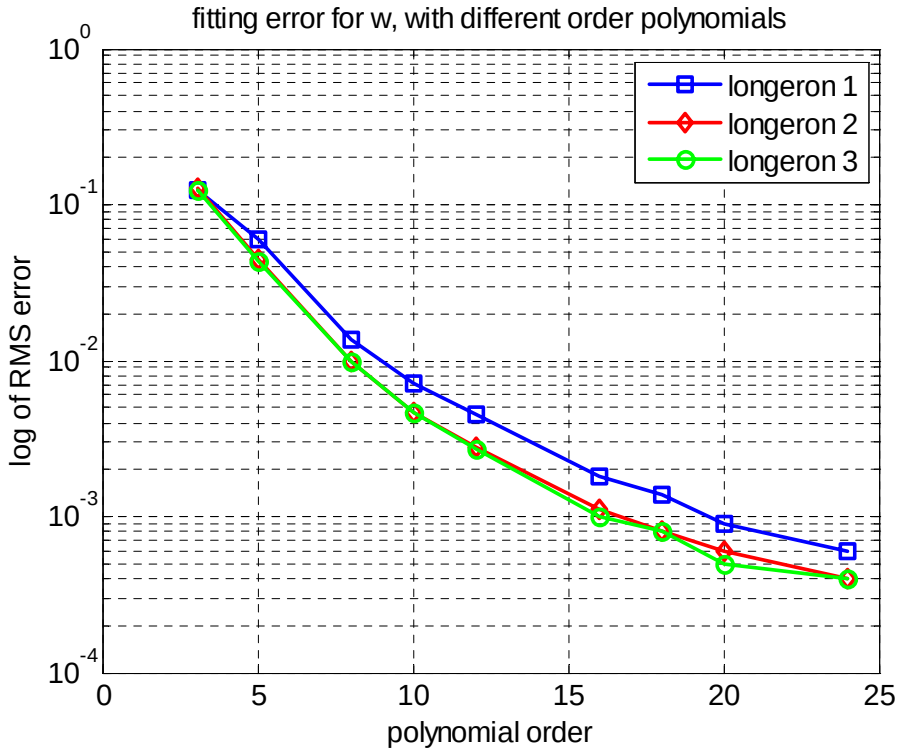

Figure 27: fitting error of "w" in log scale, with different orders of polynomial model

We also find that even for some lower modes, high order polynomial is also necessary to have a good fitting result. In Figure 28 and Figure 29, we show the relations between RMS error and mode number, when the order of polynomial are 6 and 12.

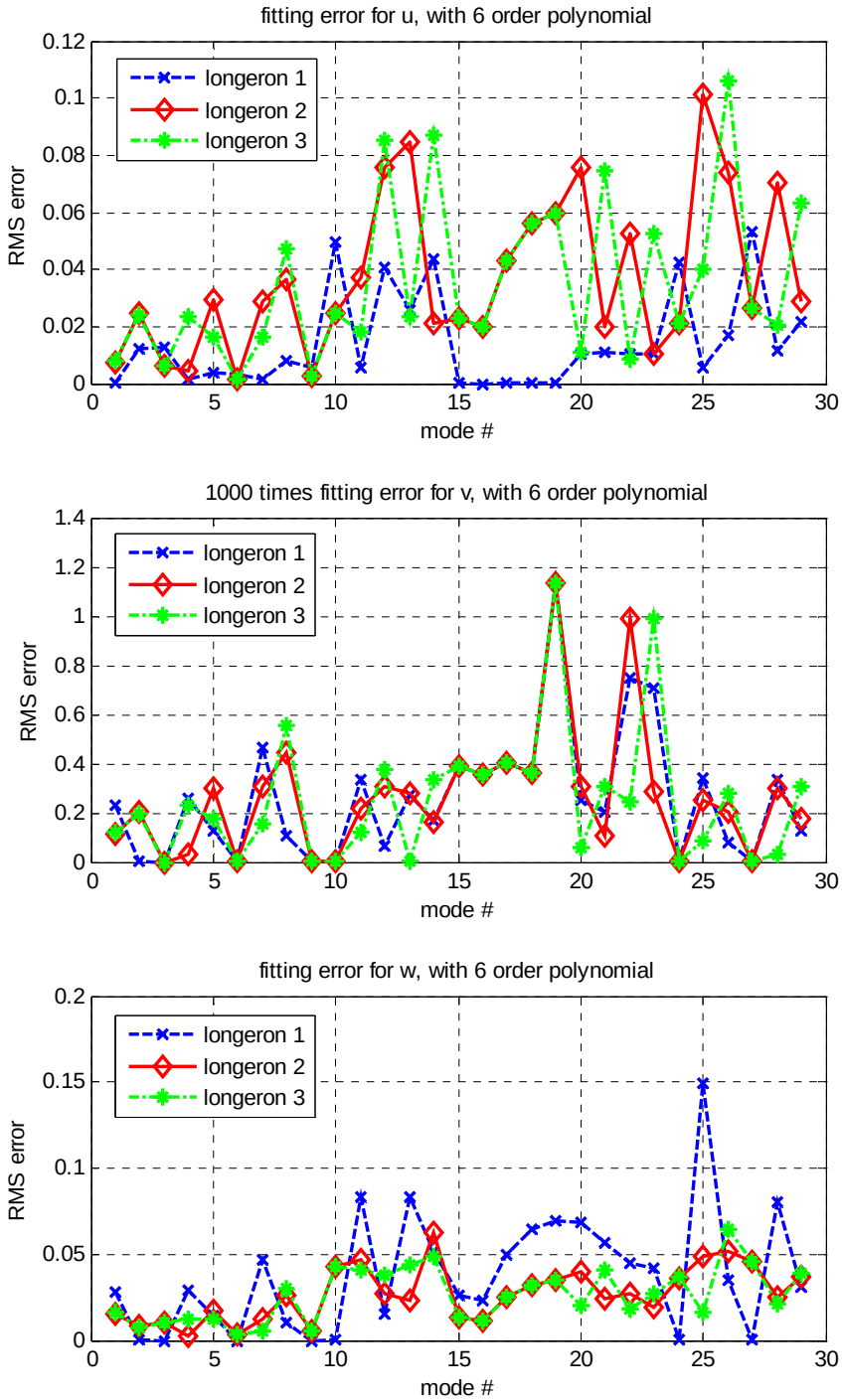

Figure 28: fitting error for different modes with a 6-order polynomial model

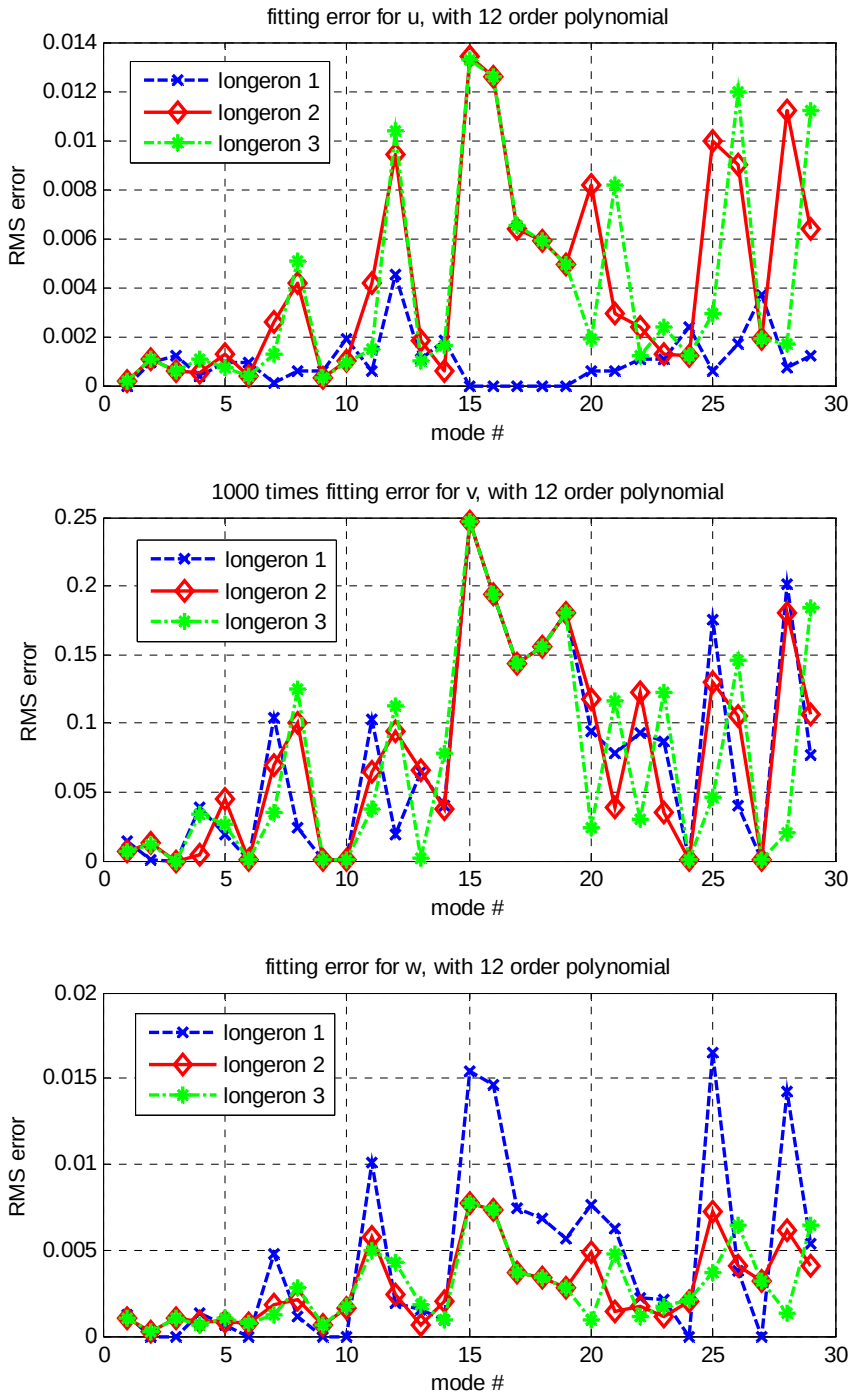

Figure 29: fitting error for different modes with a 12-order polynomial model

3.2.4. Modal function Verification

In the previous section, the polynomial fitting results are verified at all IPs. However, the results on the points other than IPs still need to be examined. One concern is that there might be erroneous overfitting oscillations due to the very high order terms in the polynomial model.

Before diving into a complex verification process, we can make a simple consideration. With the order no more than 24, there are 25 unknowns in the linear regression problem. We include 315 points in the modal displacement measurement (shown in Figure 30), which means the number of equations is much larger than the number of unknowns and consequently the regression problem is heavily over constrained. As a result, it is very unlikely that there are large oscillations among those 315 points.

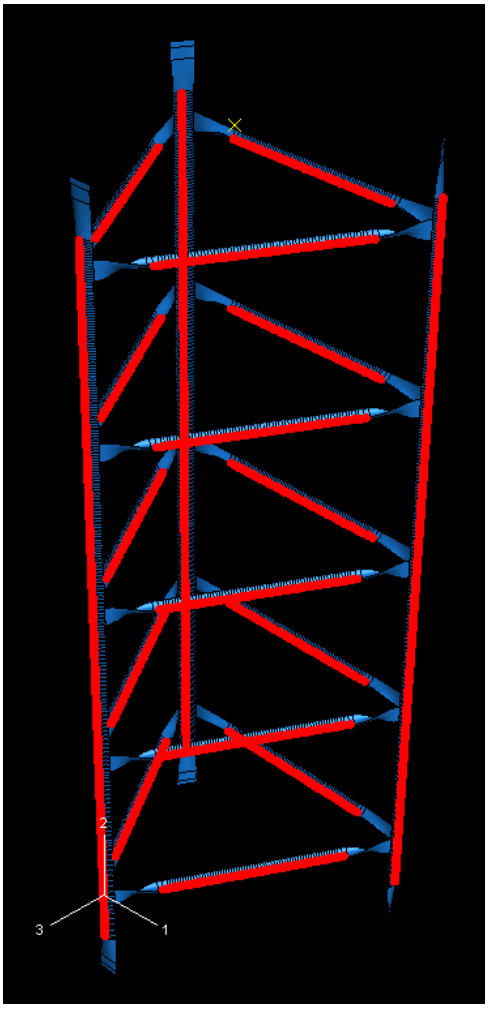

Figure 30: huge amount of points in fitting modal functions

More quantitatively, we examine the strain and displacement relationship shown in Eq.(20), Eq. (21), and Eq. (22), which means we calculate the strains from the derivatives of fitted modal displacement functions, and compare the results with ABAQUS measured strain. If there are oscillations in the fitted modal displacement functions near the IPs, the derivatives should be much larger than those of a smooth fitted function, which will introduce significant error into the estimated strains.

$$\varepsilon_{yy} = \frac{\partial v}{\partial y} \tag{20}$$

$$v = v_{stretching} - x \cdot \frac{\partial u}{\partial y} - z \cdot \frac{\partial w}{\partial y} \tag{21}$$

$$\varepsilon_{yy} = \frac{\partial v}{\partial y} = \frac{\partial v_{stretching}}{\partial y} - x \cdot \frac{\partial^2 u}{\partial y^2} - z \cdot \frac{\partial^2 w}{\partial y^2} \tag{22}$$

Eq. (20) relates the measured strain ε_{yy} (E11 in ABAQUS output notations) with vertical displacement function **v**.

We show the verification results of **v** in Figure 31 (mode #1, bending) and Figure 32 (mode #3, torsion), and we see very good estimation results.

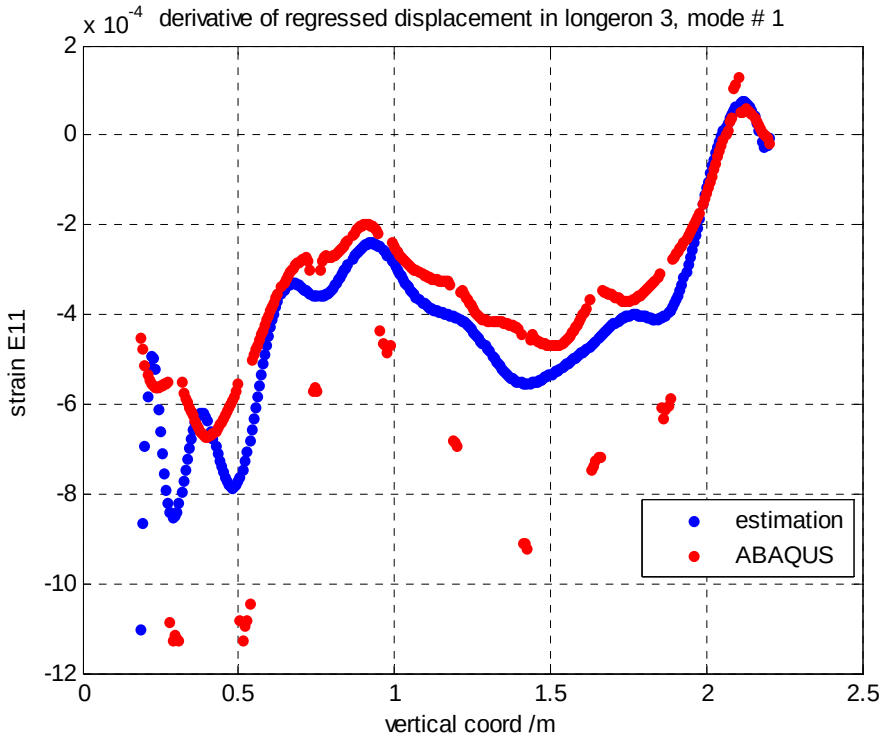

Figure 31: displacement function "**v**" verification, mode #1

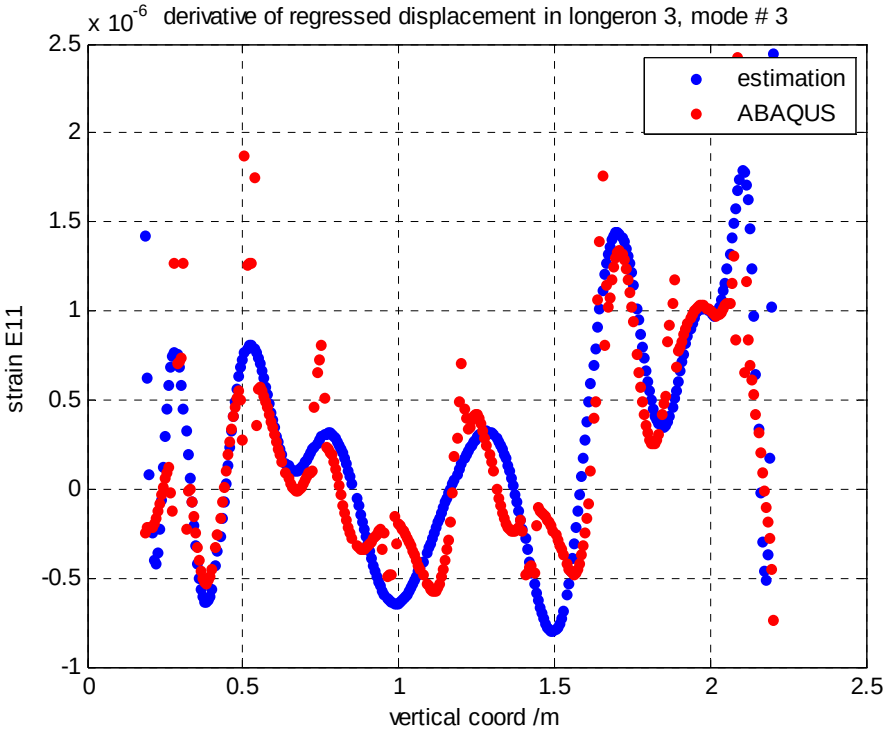

Figure 32: displacement function "**v**" verification, mode #3

Eq. (21) relates the **v** with horizontal movement **u** and **w**, where $\mathbf{v}_{streching}$ is an unknown variable meaning the vertical displacement due to pure stretching, and x and z are the offsets between the measuring points and neutral axis. Eq. (22) rewrites Eq. (20) with substitution of **v** with Eq. (21).

It is assumed in Eq. (21) that $\mathbf{v}_{streching}$ is very small, as major portion of vertical movements is induced by bending. Due to the flexibility and complexity of the frame, it is hard to determine the values of x and z offsets. For simplicity, as shown in Figure 33, we assume that these two offsets are constant during the loading process, and they are equal to the projections of the distance between measuring point and neutral axes along global 1 and 3 directions.

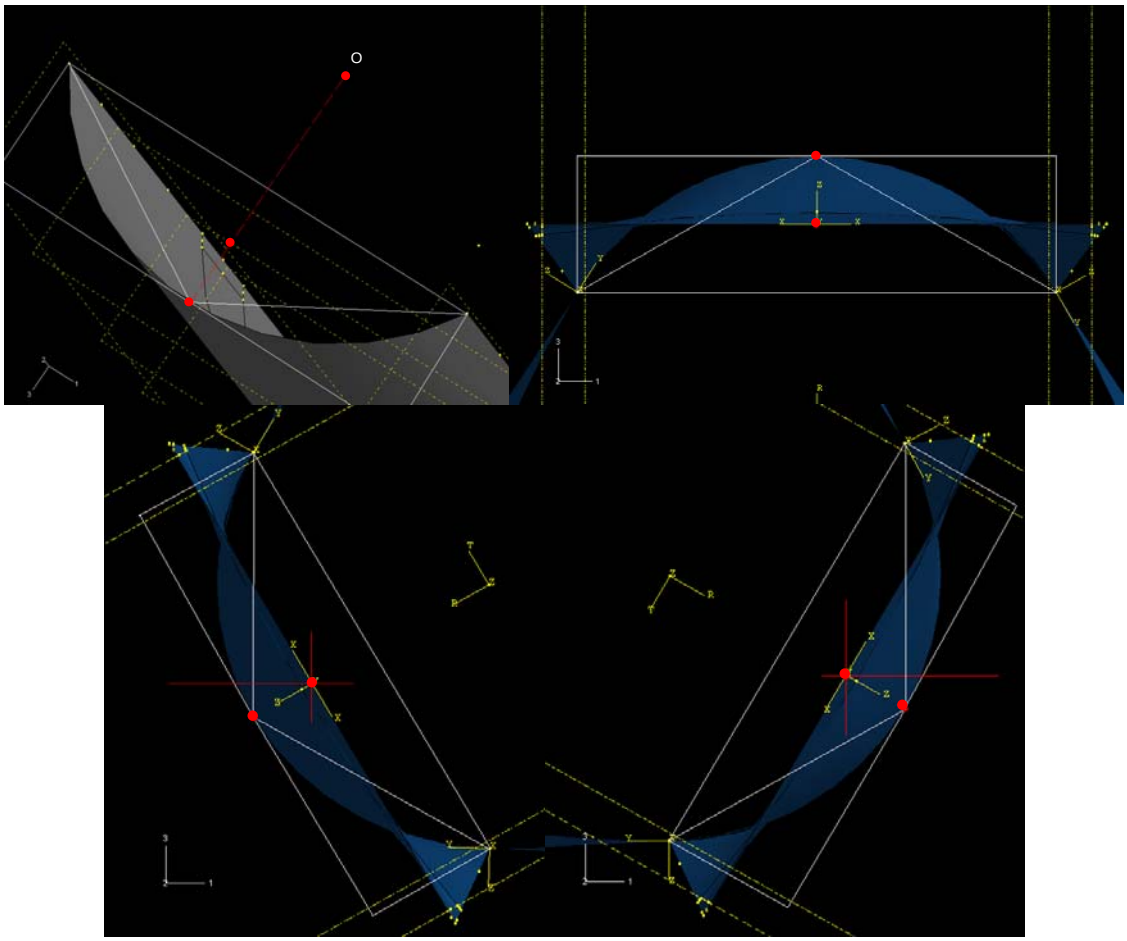

Figure 33: bending offsets illustration

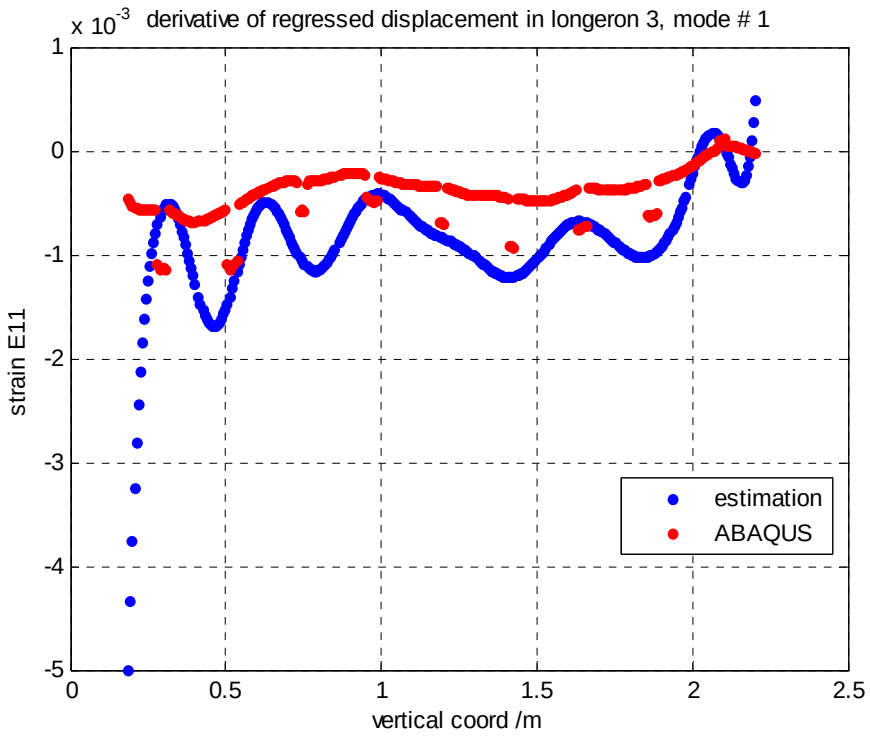

Figure 34: displacement function "**u**" and "**w**" verification, mode #1

With these two assumptions, we calculate the estimated strain according to **u** and **w** for mode #1, and show the results in Figure 34, which can be compared with the estimated strain according to **v** in Figure 31.

The estimation becomes worse than the verification result according to vertical displacements, which is because the actual offsets x and z are non-constant for different loading and location. The actually x and z values are considerably less than what we assumed at most measuring points, and consequently the magnitudes of estimated strains are larger than real values. With some errors introduced by our assumption, nevertheless the estimated strains are quite stable and within a reasonable range, which makes us confident in the fitting results of **u** and **w**.

3.2.5. Reconstructing test

We use the same 26 test cases as in the matrix approach (shown in Figure 12) to check the reconstruction results for modal approach.

The same RMS error is defined as criterion to evaluate the reconstruction for each spatial direction in the strategy of modal approach. Since we only have the displacement vector at interest points as benchmark, we evaluate reconstruction only at IPs.

$$e^{(i)} = \sqrt{\frac{1}{n}\cdot\sum_{1}^{n}\left[\left(\frac{(\mathbf{U}^{(i)}{}_{estimation} - \mathbf{U}^{(i)}{}_{ABAQUS})}{\max(\mathbf{U}^{(1)}_{ABAQUS}, \mathbf{U}^{(2)}_{ABAQUS}, \mathbf{U}^{(3)}_{ABAQUS})}\right)^2\right]}$$

$$= \sqrt{\frac{1}{n}\cdot\sum_{1}^{n}\left[\left(\frac{(\mathbf{U}^{[m](i)}\times\mathbf{W} - \mathbf{U}^{(i)}{}_{ABAQUS})}{\max(\mathbf{U}^{(1)}_{ABAQUS}, \mathbf{U}^{(2)}_{ABAQUS}, \mathbf{U}^{(3)}_{ABAQUS})}\right)^2\right]} \qquad (23)$$

$$= \sqrt{\frac{1}{n}\cdot\sum_{1}^{n}\left[\left(\frac{(\mathbf{U}^{[m](i)}\times\left[(\mathbf{E}^{[m]})^{-1}\times\mathbf{E}^{[t]}\right] - \mathbf{U}^{(i)}{}_{ABAQUS})}{\max(\mathbf{U}^{(1)}_{ABAQUS}, \mathbf{U}^{(2)}_{ABAQUS}, \mathbf{U}^{(3)}_{ABAQUS})}\right)^2\right]}$$

$$i = 1,2,3 \qquad \mathbf{U}^{(i)} \Leftrightarrow \mathbf{u}, \mathbf{v}, \mathbf{w}$$

In Eq. (23), $\mathbf{U}^{[m]}$ and $\mathbf{E}^{[m]}$ are the matrix of modal displacement and strain, and $\mathbf{W}$ is the weighting ratio vector.

Four factors influence the RMS error defined in Eq. (23): order of polynomial, number of IPs, locations of IPs and number of modes. We will discuss their effects respective in the following sections. If we use modal vector instead of continuous modal function (Eq. (23) specifically shows this instance), then order of polynomial does not affect our reconstruction results.

3.2.6. Parameter study

Order of polynomial:

We have studied the relationship between the fitting error and the order of polynomial in the section of "**3.2.3 Order selection of the polynomial model**". Convergence was achieved when the order

was increased, and for the order higher than 16, the total normalized average error in all three directions dropped lower than 10^{-3}. With the best fitting performance, 24-order polynomial model was selected.

Number of interest points:

Using the same 26 test cases and uniform distribution of IPs as described in the corresponding section of matrix approach, we perform shape reconstruction with changing number of IPs and plot the normalized RMS error averages in Figure 35.

Similarly with matrix approach, we also find the RMS errors are not strongly correlated with the number of IPs.

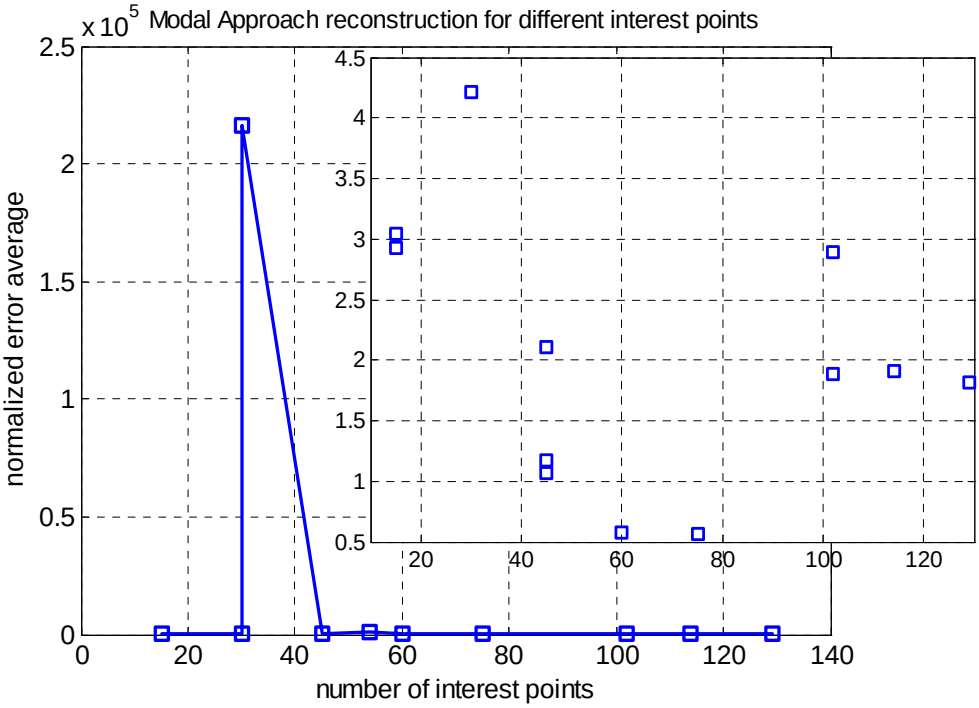

Figure 35: modal approach reconstruction for different number of interest points

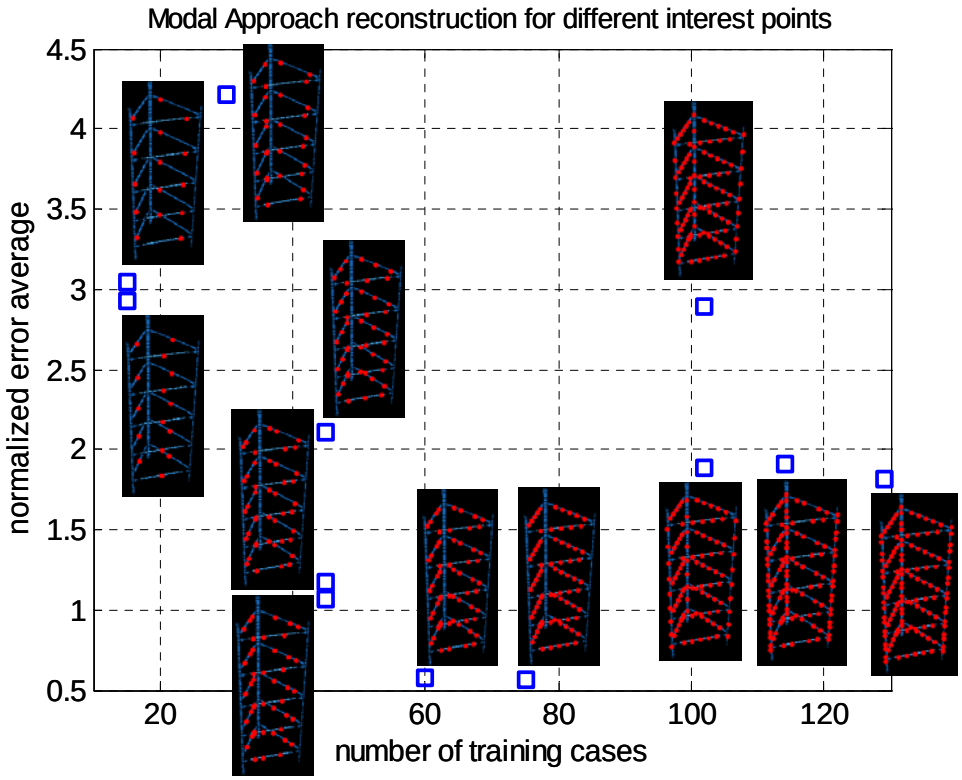

Figure 36: zooming in of Figure 35 with global views of different IPs selections

Location of interest points:

Following the method used in matrix approach, we choose different combinations of IPs from subsets of unit battens and longerons so that IPs are uniformly distributed globally, as shown in Figure 36.

Table 9: averaged error with different IP locations for modal approach

Collection #	Number of total IPs	Batten IP selection	Longeron IP selection	Average RMS error	Collection #
1	129	[1 2 3 4 5]	[1 2]	1.8172	1
2	102	[1 2 3 4 5]	[1]	1.8810	2
3	102	[1 2 3 4 5]	[2]	2.8951	3
4	75	[1 2 3 4 5]	[ ]	0.5692	4
5	114	[1 2 4 5]	[1 2]	1.9146	5
6	60	[1 2 4 5]	[ ]	0.5760	6
7	45	[1 3 5]	[ ]	2.1138	7
8	45	[1 4 5]	[ ]	1.1704	8
9	45	[1 2 4]	[ ]	1.0723	9
10	30	[1 5]	[ ]	4.2170	10
11	30	[2 4]	[ ]	216670.008	11
12	15	[3]	[ ]	2.9317	12
13	15	[2]	[ ]	2.9318	13
14	15	[5]	[ ]	3.0418	14
15	54	[ ]	[1 2]	788.0213	15

Table 10: detailed results of shape sensing errors

modal approach with IP [1:5] & [ ], 24 order polynomial											
Desc.	#	Longeron_1			Longeron_2			Longeron_3			Σ
		u	v / 1e-003	w	u	v / 1e-003	w	u	v / 1e-003	w	
c	1	0.1139	0.6574	0.1032	0.1741	1.1566	0.0850	0.3833	0.9966	0.5975	1.4598
c	2	0.0221	0.6500	0.0704	0.1503	0.2951	0.2195	0.0782	0.7773	0.0361	0.5783
c	3	0.1139	0.6574	0.1032	0.1741	1.1566	0.0850	0.3833	0.9966	0.5975	1.4598
c	4	0.3111	0.2790	0.0329	0.0480	0.6313	0.0495	0.0591	0.5009	0.0522	0.5542
c	5	0.6344	6.6217	0.6776	0.2966	1.8936	0.7403	0.1792	2.0119	0.0990	2.6376
c	6	0.0889	1.4875	0.1364	0.1713	1.4530	0.0549	0.3792	0.6682	0.5895	1.4238
d	7	0.0118	0.6064	0.0599	0.0169	0.2830	0.0466	0.0159	0.2503	0.0296	0.1818
d	8	0.1773	1.0686	0.1483	0.0395	0.6571	0.0946	0.1181	1.1316	0.3884	0.9691
d	9	0.0889	1.9400	0.2004	0.0233	0.5320	0.1261	0.0608	0.4473	0.1313	0.6337
d	10	0.0524	0.0909	0.0137	0.0490	0.5994	0.0131	0.0546	0.5175	0.0221	0.2061
p	11	0.0115	0.5794	0.1067	0.0122	0.3284	0.1033	0.0111	0.2687	0.0830	0.3290
p	12	0.1130	0.6188	0.0351	0.0403	0.9811	0.0553	0.0287	0.5617	0.0340	0.3086
p	13	0.0429	0.8115	0.0475	0.0851	0.7616	0.1333	0.0666	1.1671	0.0783	0.4564
p	14	0.0509	0.2485	0.0267	0.0673	0.5048	0.0337	0.0478	0.3014	0.0096	0.2371
b	15	0.0115	0.5491	0.0912	0.0132	0.3075	0.0867	0.0124	0.2518	0.0669	0.2830
b	16	0.1636	0.6607	0.0910	0.0887	0.1879	0.0989	0.1314	0.5305	0.0713	0.6463
b	17	0.0130	0.1810	0.0189	0.0594	0.4496	0.0165	0.0746	0.5536	0.0231	0.2067
b	**18**	**0.0111**	**0.2898**	**0.0359**	**0.0102**	**0.1902**	**0.0318**	**0.0063**	**0.0970**	**0.0258**	**0.1217**
b	19	0.0060	0.2762	0.0341	0.0108	0.0371	0.0289	0.0185	0.2366	0.0259	0.1247
b	20	0.0596	0.0454	0.0061	0.0389	0.0006	0.0672	0.0406	0.0533	0.0562	0.2687
b	21	0.0494	0.7745	0.1076	0.0154	0.4762	0.1148	0.0319	0.4547	0.0737	0.3945
b	22	0.0355	0.4924	0.0623	0.0119	0.2967	0.0816	0.0075	0.1940	0.0348	0.2346
b	23	0.2054	0.4778	0.0391	0.0651	0.2010	0.0780	0.1064	0.3270	0.1099	0.6049
b	24	0.0299	0.3322	0.0393	0.0142	0.2472	0.0465	0.0072	0.0728	0.0216	0.1594
b	25	0.0347	0.0975	0.0123	0.0443	0.3596	0.0146	0.0416	0.2579	0.0094	0.1576
b	26	0.0361	0.1883	0.0268	0.0175	0.1571	0.0202	0.0196	0.1055	0.0407	0.1614
average		**0.0957**	**0.7955**	**0.0895**	**0.0668**	**0.5440**	**0.0972**	**0.0909**	**0.5281**	**0.1272**	***0.5692***

Table 9 gives the reconstruction errors with different IP locations in modal approach. Several observations are summarized as follows.

1. Comparing collection 1, 2, 3 and 4, the best reconstruction is collection 4, which indicates that the IPs on longeron has negative effect on reconstruction accuracy in modal approach. Collection 5 and 6 also demonstrate the same tendency. Collection 15 further confirms the destructive effect of IPs on longerons.

2. Comparing collection 4 and 6, error becomes a little larger as IP#3 is not included.

3. Comparing collection 10 and 11, error blows up if subset [2 4] is used.

4. Collection 12, 13 and 14 shows that when only one IP is selected on unit batten, there is no preference in terms of error to choose [2], [3] or [5].

As a more detailed result, we list the data into Table 10 for the 26 tests with the best combination of IPs,

Number of modes:

We demonstrate the effect of number of modes on reconstruction errors in Figure 37. It is observed that when more than 10 modes are used, the reconstruction results are converged with very low errors. The slight increment of error when increase the number of mode from 15 to 29 is caused by the particularity of test cases we choose.

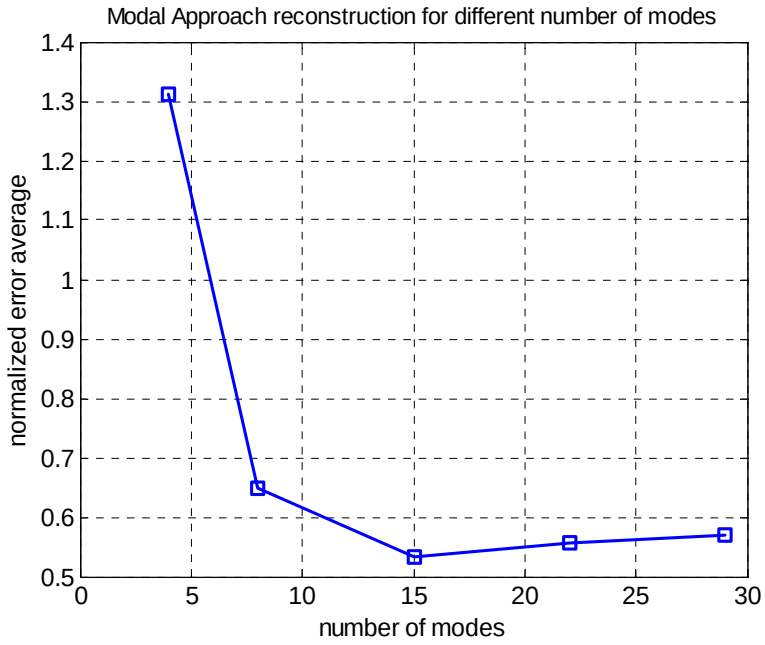

Figure 37: modal approach reconstruction for different number of modes

3.2.7. Reconstruction visualization

As an example of good reconstruction, visualizations of results of case #18 are shown in Figure 38 to Figure 41. Figure 38 depicts the loading of the case, which is defined as gravity with the direction showed by an arrow, Figure 39 gives the deformed shape of the structure, Figure 40 plots the weighting ratio of each mode and Figure 41 shows the estimated/real displacement along all three directions on longeron 1, 2 and 3.

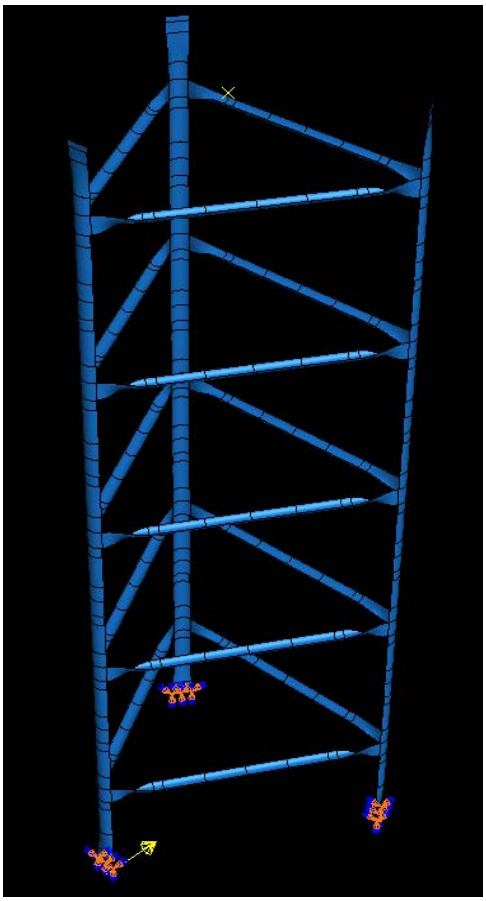

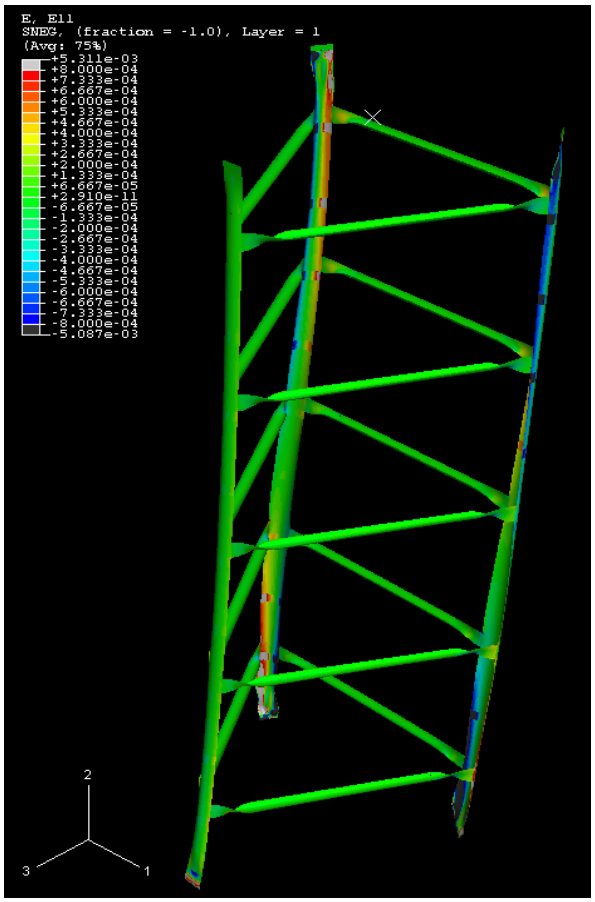

Figure 38: test case #18 loading illustration (left)

Figure 39: test case #18 deformation and strain distribution illustration (right)

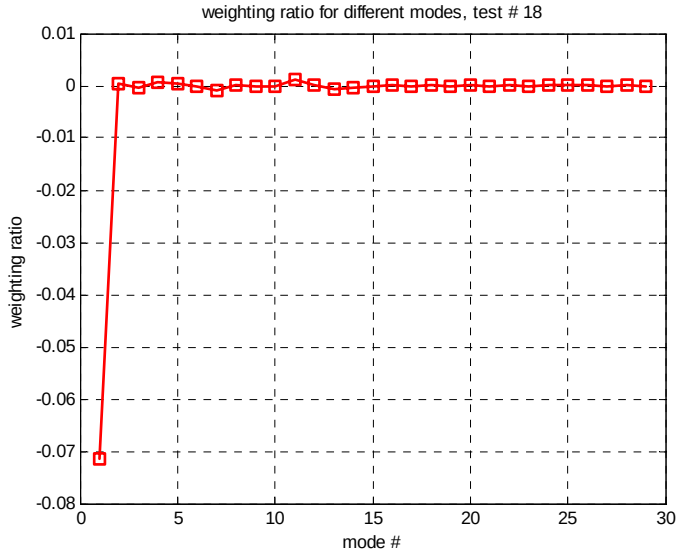

Figure 40: test case #18 weighting ratio for each mode

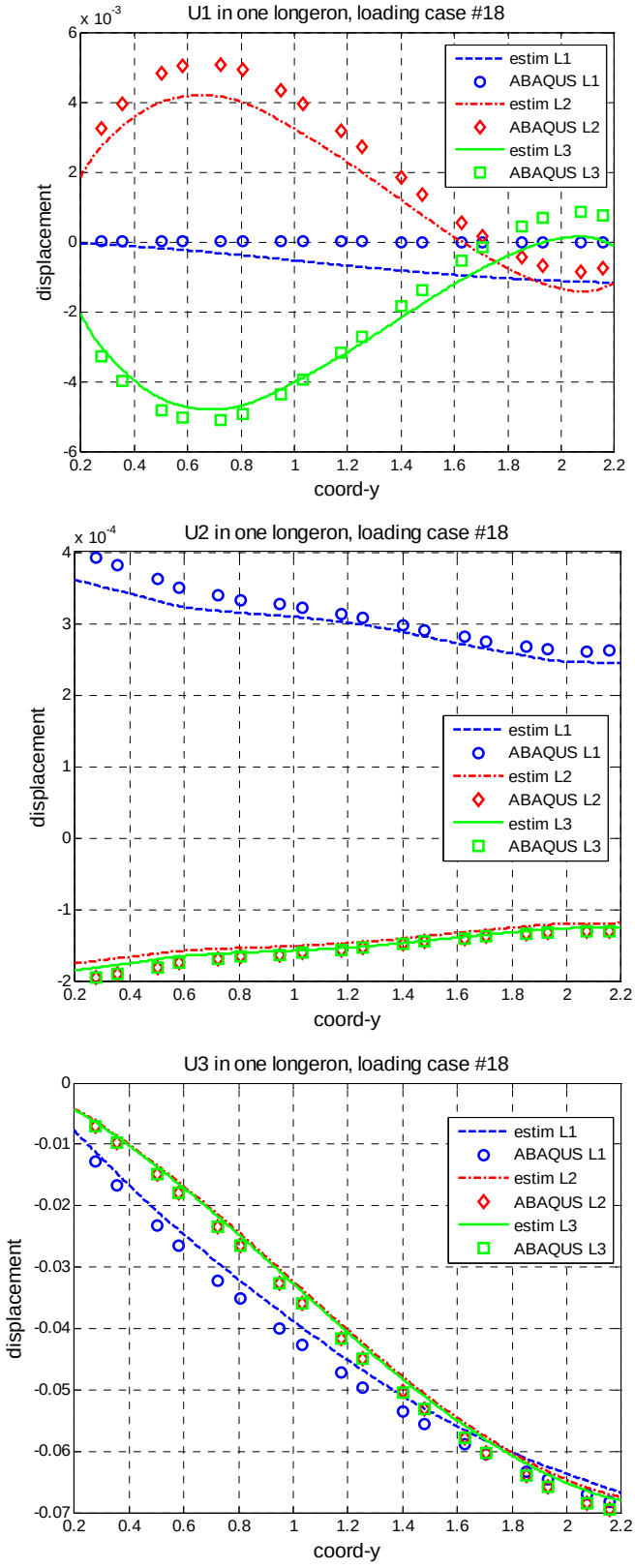

Figure 41: test case #18 displacement reconstruction curves

4. Summary and Conclusions

4.1 Comparison of the two strategies

Based on all the reconstruction results we obtained in previous sections, we compare the two reconstruction strategies in this section.

In the matrix approach, without involving mechanical understanding, we simply consider the 3-D displacements under a loading as linear combinations of the corresponding strains. In contrast, we project the strain measurements to the different mode in the modal approach, and this modal analysis contains mechanics of the structure itself. Generally speaking, modal approach can achieve better reconstruction than matrix approach, as shown in Figure 42.

However, we find the matrix approach outperform the modal approach for some concentrated forces tests. That is because in the matrix approach, the system is trained with concentrated force, so it can have good performance in the tests with a similar loading as those trainings, even better than modal approach.

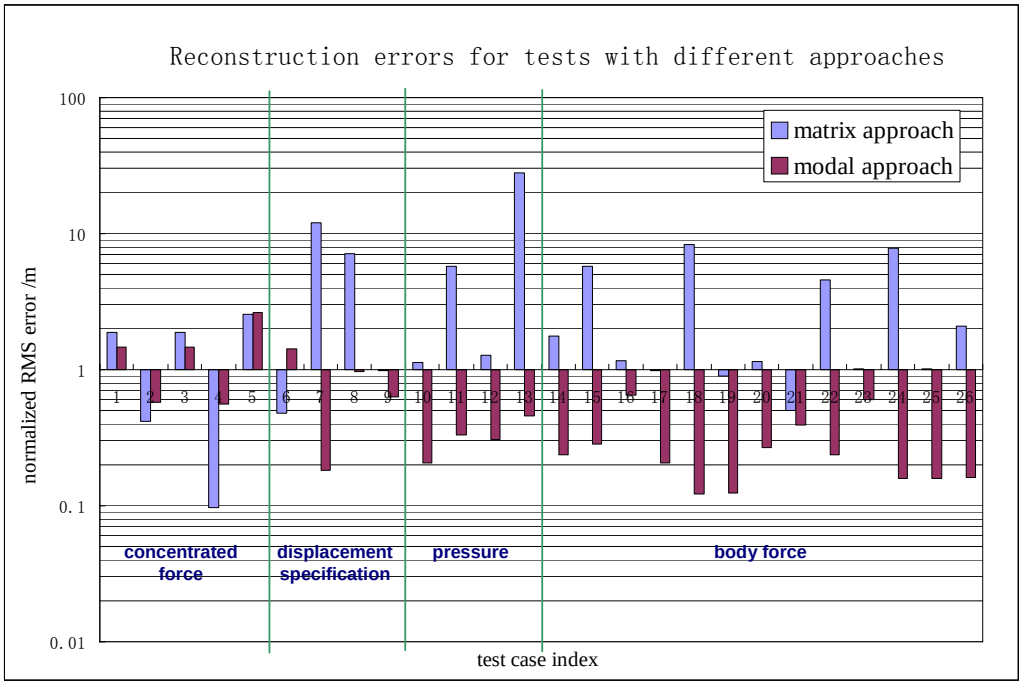

Figure 42: Comparison between the two strategies

4.2 Conclusions

Comparing the two approaches of shape reconstruction in a complex flexible structure, we conclude our work as follows.

- In matrix approach, we approximate the static displacements as linear combinations of strains after training the system in a self learning mode. With a matrix representing the linear mapping, we found that if sufficient training cases are made, there will be a satisfactory shape reconstruction.

    - There are three major factors affecting the shape reconstructing results of matrix approach: amount of training cases, amount of IPs, and the location of those IPs.

    1. Generally speaking, the more we trained the system, the better of our reconstruction results. Especially when the test case is similar to some training cases, good shape reconstruction can be achieved.

    2. The amount of IPs does not affect the reconstruction significantly if it is more than a certain value.

    3. The location of IPs is the most dominant factor in the matrix approach. A good architecture of IPs optimizes the reconstruction process in terms of cost and accuracy.

- In modal approach, we select modal functions as a set of basis to decompose the strain measurements, and regard the weighting ratio of each mode as the connection between strain and displacement, so that structural shape can be reconstructed according to strain measurements.

    - There are three major factors affecting the shape reconstructing results of modal approach: number of modes included in the superposition, amount of IPs, and the location of those IPs.

    1. Generally, the more the modes are included in the superposition, the better the reconstruction shall we obtain.

    2. The amount of IPs does not affect the reconstruction very much, but a necessary number of points should be guaranteed to capture the deformation characteristics.

3. The location of IPs is the essential factor dominating the reconstruction. A good architecture of IPs optimizes the reconstruction process in terms of cost and accuracy.

- There is no mechanical methodology in the matrix approach, while the modal approach is based on the basic dynamic knowledge, and more complex to model, hence more possible sources of error.

- Overall the modal approach is more accurate than the matrix approach, but for tests with concentrated forces, the matrix approach does a better job, because the system is trained in this way.

- The modal approach is more robust since it requires only mode shape estimation, and is only determined by the sensor topology without learning process required or knowledge of loads.

- There is trade-offs to be considered between accuracy, the ability to train, and complexity of modeling.

4.3. Future Work

Thermal gradients on this structure should be considered in a more realistic scenario since the truss is exposed to the radiation of the sun. More importantly, the thermal gradient induces extra strain when the measurement is performed. We plan to characterize and analyze the thermal characteristics, as an improvement of current shape sensing strategies.

The fiber Bragg gratings are actually attached to the boom by epoxy, which introduces a load-dependent shear transfer. We will analyze and evaluate the effects of the shear transfer on reconstruction accuracy and modify our shape sensing model accordingly in the next phase.

The strategies can be implemented rapidly into operational software, and a quasi-real time shape determination can be performed.

Experimental investigation on a model boom at Air Force Research Lab will be considered. Instead of using ABAQUS finite element simulation, we will further verify our approaches with real strain and displacement data.

Reference

[1]. Arritt, B., Murphey, T., Dumm, H., Pollard, E., and Klimcak, C., "Demonstration of the Use of Fiber-Optics, with Integrated Fiber-Bragg Gratings, for Shape Determination of Large Deployable Structures," 48th AIAA/ASME/ ASCE/AHS/ASC Structures, Structural Dynamics, and Materials Conference, Honolulu, Hawaii, (Apr. 23-26, 2007).

[2]. Friebele, E.J., et al., "Optical Fiber Sensors for Spacecraft Applications," Smart Materials and Structures, 8, 813-838 (1999).

[3]. Friebele, E. J., Putnam, M. A., Patrick, H. J., Kersey, A. D., Greenblatt, A. S., Ruthven, G. P., Krim, M. H. and Gottschalck, K. S., "Ultrahigh-sensitivity fiber-optic strain and temperature sensor, " Opt. Lett. 23 222–4 (1998).

[4]. Beraldin, et al., "Eye-safe digital 3-D sensing for space applications," Opt. Eng. 39(1) 196–211 (2000).

[5]. Reich, C., Ritter, R. and Thesing, J., "3-D shape measurement of complex objects by combining photogrammetry and fringe projection," Opt. Eng. 39(1) 224–231 (January 2000).

[6]. Blandino J.R. et al., "Three-Dimensional Shape Sensing for Inflatable Booms," 46th AIAA/ASME/ASCE/AHS /ASC Structures, Structural Dynamics & Materials Conference, Austin, Texas, (April 18 – 21, 2005).

[7]. Lopez-Higuera, J.M., [Handbook of Optical Fibre Sensing Technology], John Wiley and Sons (West Sussex, UK), (2002).

[8]. Chen, F., Brown, G.M., Song, M., "Overview of three-dimensional shape measurement using optical methods," Optical Engineering, 39(1), 10–22, (January 2000).

[9]. Brown, G.M. and Chen, F., "Optical Methods for Shape Measurement," Optical Engineering, Vol.39(No.1), (January 2000).

[10]. Navalgund, R.R., et al., "Remote sensing applications: An overview," CURRENT SCIENCE, VOL. 93, NO. 12, 25 (DECEMBER 2007).

[11]. Tien, J.Y., et al., "Technology Validation of the Autonomous Formation Flying Sensor for Precision Formation Flying," Aerospace Conference, Proceedings. 2003 IEEE. Volume 1, March 8-15, 2003 Page(s): 1 – 140.

[12]. Mettler, E., et al., "Dynamics and Control of a 25-Meter Aperture Virtual Structure Gossamer Telescope in GEO," AIAA/AAS Astrodynamics Specialist Conference and Exhibit, Monterey, California, (Aug. 5-8, 2002).

[13]. Sergei Azernikov, Anath Fischer, "Efficient surface reconstruction method for distributed CAD," Computer-Aided Design 36 (2004) 799–808.

[14]. Mark Moll, Michael A. Erdmann, "Dynamic Shape Reconstruction Using Tactile Sensors," Proceedings of the 2002 IEEE International Conference on Robotics & Automation Washington DC, May 2002.

[15]. Klute, S., et al., “Fiber-Optic Shape Sensing and Distributed Strain Measurements on a Morphing Chevron,” 44th AIAA Aerospace Sciences Meeting and Exhibit, Reno, Nevada, Jan. 9-12, 2006.

[16]. Lynch, J.P., “An overview of wireless structural health monitoring for civil structures,” Royal Society of London Transactions Series A, vol. 365, Issue 1851, p.345-372.

[17]. Sazonov, E., Janoyan, K., and Jha, R., “Wireless Intelligent Sensor Network for Autonomous Structural Health Monitoring,” Proceedings of SPIE’s Annual International Symposium on Smart Structures and Materials, San Diego, CA, 2004.

[18]. Charles. R. F., et al., “SENSING AND SENSOR OPTIMIZATION ISSUES FOR STRUCTURAL HEALTH MONITORING,” 23rd Aerospace Testing Seminar, October 10-12, 2006 Manhattan Beach, CA.

[19]. David Culler, Deborah Estrin, and Mani Srivastava, “Guest Editors' Introduction: Overview of Sensor Networks,” IEEE Computer, Vol. 37, No. 8, August 2004.

[20]. François Blais, “Review of 20 years of range sensor development,” Journal of Electronic Imaging 13(1), 231–240 (January 2004).

[21]. Michael Hill-King, “Smart structures through embedding optical fibre strain sensing,” Smart Materials Bulletin, May 2001.

[22]. ALAN D. KERSEY, “A Review of Recent Developments in Fiber Optic Sensor Technology,” OPTICAL FIBER TECHNOLOGY 2, 291–317 (1996).

[23]. Bartley-Cho, J.D., et al., “Shape estimation of deforming structures,” 42nd AIAA/ASME/ASCE/AHS/ASC Structures, Structural Dynamics, and Materials Conference and Exhibit, Seattle, WA, Apr.16-19, 2001.

[24]. Ganotra, D. “Object reconstruction in multilayer neural network-based profilometry using grating structure comprising two regions with different spatial periods,” Optics and Lasers in Engineering, 42, p179 – 192 (2004).

[25]. Igwe, P.C., et al., “Shape Morphing and Reconstruction Using A Self-Organizing Feature Map,” 2006 International Joint Conference on Neural Networks, Vancouver, BC, Canada, July 16-21, 2006.

[26]. Bruno, R., et al., “Shape estimation from incomplete measurements: a neural-net approach,” Smart Mater. Struct. 3, p92-97(1994).

[27]. Bogert, P., et al., “Structural Shape Identification from Experimental Strains Using a Modal Transformation Technique,” 44th AIAA/ASME/ASCE/AHS/ASC Structures, Structural Dynamics, and Materials Conference, Norfolk, Virginia, Apr. 7-10, 2003.

[28]. Kirby, G.C., et al., “Strain-based Shape Estimation Algorithms for a Cantilever Beam,” Proceedings of the International Society for Optical Engineering Conference, March 1997.

[29]. Foss, G.C., and Haugse, E.E., “Using Modal Test Results to Develop Stain to Displacement Transformations,” 13th International Modal Analysis Conference, pp 112-118, February 1995.

[30]. Bernasconi, O., and Ewins, D.J., “Application of Strain Modal Testing to Real Structures,” 6th International Modal Analysis Conference, vol.2, pp.1453-1464, 1998.

[31]. Audette, M.A. et al., “An algorithmic overview of surface registration techniques for medical Imaging,” Medical Image Analysis 4, p201–217, (2000).